Simulations of Ellipsoidal Primordial Black Hole Formation

Albert Escrivà[a] , **Chul-Moon Yoo**[a]

[a]Division of Particle and Astrophysical Science, Graduate School of Science, Nagoya University. Nagoya 464-8602, Japan

E-mail: escriva.manas.albert.y0@a.mail.nagoya-u.ac.jp, yoo.chulmoon.k6@f.mail.nagoya-u.ac.jp

Abstract. We perform $3+1$ relativistic numerical simulations to study primordial black hole (PBH) formation from the collapse of adiabatic super-horizon non-spherical perturbations generated from curvature fluctuations obeying random Gaussian statistics with a monochromatic power spectrum. The matter field is assumed to be a perfect fluid of an equation of state $w := P/\rho = $ const. with P and ρ being the pressure and the energy density, respectively. The initial spatial profile of the curvature perturbation is modeled with the amplitude μ and non-spherical parameters e (ellipticity) and p (prolateness) according to peak theory. We focus on the dynamics and the threshold for PBH formation in terms of the non-spherical parameters e and p. We find that the critical values (e_c, p_c) with a fixed value of μ closely follow a superellipse curve. With $p = 0$, for the range of amplitudes considered, we find that the critical ellipticity for non-spherical collapse follows a decaying power law as a function of $(\mu - \mu_{c,sp})$ with $\mu_{c,sp}$ being the threshold for the spherical case. Our results also indicate that, for both cases of $w = 1/3$ and $w = 1/10$, small deviations from sphericity can avoid collapsing to a black hole when the amplitude is near its critical threshold. Finally we discuss the significance of the ellipticity on the rate of the PBH production.

Contents

1 Introduction

Primordial black holes (PBHs), if they exist, are black holes that could have been formed in the early Universe [1–5] (see [6–11] for reviews covering different perspectives). A PBH results from the collapse of a sufficiently large over-density in the early universe, much before the moment of matter-radiation equality, and therefore, their existence can be an evidence of the existence of primordial inhomogeneities. Interestingly, PBHs may constitute a significant fraction of the dark matter [12] (especially in the so-called asteroid mass range) and explain different cosmic conundra [13]. Currently, PBHs have not been detected so far, but future gravitational wave observations may establish their existence (in particular if their mass is lower than a solar mass)[14–16] and quantify their role in the dark matter.

Various mechanisms can lead to the production of PBHs (see [10] for a comprehensive list). Among these, one of the most widely studied and frequently considered is the formation of PBHs from the collapse of large curvature fluctuations generated during inflation. These fluctuations, upon re-entering the cosmological horizon at sufficiently late times, can collapse to form PBHs if they are over a certain threshold. From now on, we will focus on this scenario through this work.

To accurately estimate the abundance of PBHs in our Universe, it is essential to clarify the initial conditions that lead to their formation. Particularly, determinating the threshold is essential for the abundance estimation as it is exponentially sensitive to the threshold [4]. The threshold estimation typically requires relativistic numerical simulations. Most studies on simulation of PBH formation have focused on spherically symmetric systems (see [17] for a comprehensive review and references therein) for what we have nowadays a relatively solid

understanding. In contrast, our understanding of PBH formation in non-spherical scenarios currently remains limited, with only a few studies numerically addressing this issue [18–21] (see also [22–25] for non-spherical collapse of perfect fluids in asymptotically flat spacetimes).

For PBHs formed during the radiation-dominated era of the Universe, the assumption of spherical symmetry is well justified within the framework of peak theory [26]. In this context, large peaks in curvature fluctuations which are so rare that they are not overproduced beyond the dark matter density tend to be nearly spherical. However, even for such large peaks, the most likely configuration is not perfectly spherical [26]. Instead, small deviations from sphericity are typical, leading to an ellipsoidal shape characterized by parameters known as "ellipticity" (e) and "prolateness" (p) following a probability distribution. Regarding the PBH formation with the initial amplitude slightly above the threshold for which critical behavior [27] is relevant, it is not entirely clear how small deviations from sphericity impact the critical behavior of the collapse.

Non-spherical PBH formation during a radiation-dominated Universe was studied in [18] through $3 + 1$ numerical simulations, considering a case with spheroidal ($p = \pm e$) initial curvature fluctuation. The results showed that, for a typical fluctuation amplitude and a Gaussian spatial profile, the threshold for non-spherical collapse is not significantly modified compared with the spherical case. In this work, we aim to consider a different curvature profile sourced by a monochromatic power spectrum following peak theory and determine the threshold values for e and p. We further explore how these thresholds vary with different fluctuation amplitudes. Clarifying the PBH formation condition including the parameters e and p is crucial for statistically estimating the impact of non-spherical effects on the PBH mass function. This can also be a starting point for the generalization of analytical threshold estimations for non-spherical collapse, taking into account the values of e and p as the parameters characterizing the initial profile, as done in [28, 29] in the case of spherical symmetry.

In the case of a soft equation of state, the reduction in pressure gradients may lead the non-sphericities to modify the gravitational collapse substantially, being the case of a dust-dominated epoch a clear example where non-spherical effects are crucial [20, 30–32] (see also [33–37] where a dust epoch is modulated with scalar fields). It is well known, for instance, that for spherically symmetric configurations, the threshold is significantly affected by the equation of state parameter [29, 38]. The threshold of PBH formation substantially decreases due to the reduction of pressure gradients for a smaller value of $w := P/\rho$, where P and ρ are the pressure and energy density, respectively.

Non-spherical effects may be relevant for some physically well-motivated scenarios where soft equations of state are considered and predictions of the mass function of PBHs may be contrasted with the gravitational wave spectrum of induced gravitational waves (see [39] for a review) and/or with merger rates of PBH binaries [40, 41]. The softening can be due to a still unknown phase transition or to the standard thermal history of the Universe [42] when particles become non-relativistic. For instance, the softening of the equation of state due to the QCD crossover about $\sim 10^{-5}$s after the Big Bang [43–45] might cause a significant number of PBHs in the solar mass range [46–55]. Another possibility is from crossovers beyond standard model theories that may induce a significant softening of the equation of state [56, 57]. In addition, several scenarios with $w \neq 1/3$ have also been considered in the context of the PTA signal [58, 59] and its counterpart with PBHs [60–66].

So far, spherical symmetry is assumed to determine the threshold for PBH formation and to statistically compute the PBH mass function, which is then used to place observational constraints on the PBH scenario. An open question in this context is whether deviations

from spherically symmetric fluctuations can significantly alter the threshold for black hole formation, particularly for a soft equation of state. For stiff equations of state ($w > 1/3$), it is generally expected that stronger pressure gradients would make deviations from sphericity less impactful than in the radiation case ($w = 1/3$), although a numerical confirmation would be desirable. If deviations from spherical symmetry do have a more significant effect for softer equations of state than radiation, careful simulations are required for various non-spherical configurations to ensure accurate predictions.

Our investigation aims to study the dependence of the dynamics and the threshold of the initial amplitude for black hole formation on the non-spherical parameters e and p, in both radiation-dominated Universe ($w = 1/3$) and for a softer equation of state ($w = 1/10$). This will help us determine whether non-spherical effects should be considered when calculating the PBH formation threshold or if estimates assuming spherical symmetry are sufficiently accurate in realistic scenarios. For that purpose, we will employ relativistic $3+1$ numerical simulations to track the gravitational collapse of the super-horizon curvature fluctuations. We will consider the curvature fluctuation with a monochromatic power spectrum, whose results are expected to apply to a sharp-peaked spectrum as well. Throughout this work, we will use geometrized units $c = G = 1$.

2 Deviation from sphericity of the initial curvature perturbation in peak theory

In this section, we provide some details about the peak theory to obtain the typical profile of the curvature perturbation obeying a random Gaussian statistics, including a deviation from sphericity. We briefly review and follow [26].

Since the initial curvature perturbation is supposed to be a random Gaussian field, it is totally characterized by the power spectrum $P_\zeta(k)$, defined by

$$\langle \zeta(\mathbf{k})\, \zeta(\mathbf{k}') \rangle = \frac{2\pi^2}{k^3} \mathcal{P}_\zeta(k)(2\pi)^3 \delta^{(3)}(\mathbf{k} + \mathbf{k}'), \tag{2.1}$$

where $\mathbf{k}$ denotes the wavenumber vector and k is its modulus. The variance σ_0^2 is given by

$$\langle \zeta^2 \rangle \equiv \sigma_0^2 = \int \frac{dk}{k} P_\zeta(k). \tag{2.2}$$

We also define the n-th gradient moments of the power spectrum as follows:

$$\sigma_n^2 = \int k^{2n} P_\zeta(k) d\ln k. \tag{2.3}$$

We can introduce the normalized two-point correlation function of $\zeta(\vec{r})$ as

$$\psi(r) \equiv \frac{1}{\sigma_0^2} \langle \zeta(r)\zeta(0) \rangle = \frac{1}{\sigma_0^2} \int P_\zeta(k) \operatorname{sinc}(kr) \frac{dk}{k}. \tag{2.4}$$

We denote the normalized height of the peak of ζ as $\nu = \zeta(\vec{r} = 0)/\sigma_0$, and introduce the correlator $\gamma \equiv \sigma_1^2/(\sigma_0\sigma_2)$, which depends on the power spectrum $\mathcal{P}_\zeta$. Let's consider the immediate neighbour of ζ around the peak value at $\vec{r} = 0$ with a Tayor expansion up through the second order as

$$\zeta(\vec{r}) \approx \zeta(\vec{r} = 0) - \sum_l \lambda_l \frac{r_l^2}{2}, \tag{2.5}$$

where λ_l are the eigenvalues of $-\partial_i \partial_j \zeta$ and we have considered that the axes are oriented along its principal direction[1] with r_l being the cartesian coordinates. We can also arrange λ_l, so that $\lambda_1 \geq \lambda_2 \geq \lambda_3$ by considering the rotation of the axes without loss of generality. Around the peak, the contours of $\zeta(\vec{r})$ are described by the ellipsoids given by $\zeta(\vec{r} = 0) - \zeta(\vec{r}) \approx \sum_l r_l^2/(1/\lambda_l) = \text{const.}$ with the radius along each axis being proportional to $1/\sqrt{\lambda_l}$. The shape of the ellipsoid is characterized by

$$e = \frac{\lambda_1 - \lambda_3}{2\sum_i \lambda_i}, \qquad p = \frac{\lambda_1 - 2\lambda_2 + \lambda_3}{2\sum_i \lambda_i}. \tag{2.6}$$

The parameters e ("ellipticity") and p ("prolateness") are in the range $0 \leq e \leq 1/2$ and $-e \leq p \leq e$. For instance, if $(\lambda_1 - \lambda_2) - (\lambda_2 - \lambda_3) > 0 \Leftrightarrow p > 0$, the shape is oblate (pancake like) while it is prolate (cigar like) for $p < 0$. It is also common to define "spheroids" as ellipsoids with two equal eigenvalues.

The values of e and p follow a specific probability distribution, which we will explore next. For instance, the probability density vanishes for $p = e$ and $p = -e$, which correspond to oblate and prolate spheroids, respectively. That is, approximately spheroidal configurations are improbable. Let's now introduce the Gaussian distributed variable $\xi \equiv -\nabla^2 \zeta\big|_{\vec{r}=0}/\sigma_2 = \sum_i \lambda_i/\sigma_2$, where we used Eq.(2.5).

Solving Eqs.(2.6) to obtain λ_i in terms of e and p, we obtain

$$\lambda_1 = \frac{\xi \sigma_2}{3}(1 + 3e + p),$$
$$\lambda_2 = \frac{\xi \sigma_2}{3}(1 - 2p), \tag{2.7}$$
$$\lambda_3 = \frac{\xi \sigma_2}{3}(1 - 3e + p).$$

Making some algebra and using the typical trigonometric relations, we obtain[2],

$$\zeta(r) \approx \zeta(\vec{r} = 0) - \frac{\xi \sigma_2}{3} \frac{r^2}{2} \left[1 + A(e, p)\right], \tag{2.8}$$

where

$$A(e, p) = 3e \left[1 - \sin^2 \theta(1 + \sin^2 \phi)\right] + p \left[1 - 3\sin^2 \theta \cos^2 \phi\right] \tag{2.9}$$

with the convention of spherical coordinates adopted in [26]:

$$x_1 = z = r \cos \theta,$$
$$x_2 = x = r \sin \theta \cos \phi, \tag{2.10}$$
$$x_3 = y = r \sin \theta \sin \phi.$$

The parameters e and p follow a normalized probability distribution $\mathcal{P}_{e,p}$ for fixed ν and ξ, which is given by (see Eq.(7.6) in [26])

$$\mathcal{P}_{\text{e,p}}(e, p \mid \nu, \xi) = \frac{3^2 5^{5/2}}{\sqrt{2\pi}} \frac{\xi^8}{f(\xi)} \exp\left\{-\frac{5}{2}\xi^2(3e^2 + p^2)\right\} W(e, p), \tag{2.11}$$
$$W(e, p) = (1 - 2p)\left[(1 + p)^2 - (3e)^2\right] e(e^2 - p^2)\chi(e, p),$$

---

[1] Even if this is not the case, so that $\zeta(\vec{r}) = \zeta(\vec{r} = 0) + \sum_i \partial_i \partial_j \zeta \frac{r_i r_j}{2}$, the symmetric coefficient matrix of the second order can always be diagonalized through a rotation transformation.

[2] Acording to our computations, it seems there is a typo in [26] at Eq.(7.4), the expansion at second order of the field should have an extra factor 3 in the denominator.

where $f(\xi)$ is given by

$$f(\xi) = \frac{1}{2}\xi(\xi^2 - 3)\left(\mathrm{erf}\left[\frac{1}{2}\sqrt{\frac{5}{2}}\xi\right] + \mathrm{erf}\left[\sqrt{\frac{5}{2}}\xi\right]\right)$$
$$+ \sqrt{\frac{2}{5\pi}}\left[\mathcal{C}_1(\xi)\exp\left\{-\frac{5}{8}\xi^2\right\} + \mathcal{C}_2(\xi)\exp\left\{-\frac{5}{2}\xi^2\right\}\right] \tag{2.12}$$

with

$$\mathcal{C}_1(\xi) = \frac{8}{5} + \frac{31}{4}\xi^2 \ , \ \ \mathcal{C}_2(\xi) = -\frac{8}{5} + \frac{1}{2}\xi^2, \tag{2.13}$$

and $\chi(e,p)$ is defined as

$$\begin{cases} \chi = 1, & 0 \le e \le 1/4, -e \le p \le e, \\ \chi = 1, & 1/4 \le e \le 1/2, -(1-3e) \le p \le e, \\ \chi = 0, & \text{otherwise.} \end{cases} \tag{2.14}$$

This expression does not explicitly depend on ν, and the domain with a non-vanishing value is restricted to $|p| \le e$ and $e \ge 0$. Specifically, the allowed domain (e,p) is the interior of a triangle bounded by the points $(0,0)$, $(1/4, -1/4)$ and $(1/2, 1/2)$. The mean values of $\langle e \rangle$ and $\langle p \rangle$ with $\mathcal{P}_{e,p}$ can be computed analytically and are shown in the appendix A. For high peaks, the mean values $\langle e \rangle$ and $\langle p \rangle$ are small, and high peaks are more spherically symmetric than lower ones. Despite that, the most likely values are not exactly zero, i.e., a small deviation from sphericity likely to exist in general (see Fig.1). Notice that the mean value of p is much smaller than e for large ξ.

We now focus on obtaining the typical profile of the curvature fluctuation $\bar{\zeta}$ characterized by fixed values of the parameters (ν, ξ, e, p). Euler angles are fixed, so that the coordinate axes are along the principle axes of $-\partial_i\partial_j\zeta$. Then we obtain (see (7.8) in Ref. [26])

$$\frac{\bar{\zeta}}{\sigma_0} = \frac{\nu}{1-\gamma^2}\left(\psi + R_s^2\frac{\nabla^2\psi}{3}\right) - \frac{\xi/\gamma}{(1-\gamma^2)}\left(\gamma^2\psi + \frac{R_s^2\nabla^2\psi}{3}\right) + \frac{5}{2}R_s^2\left(\frac{\xi}{\gamma}\right)\left(\frac{\psi'}{r} - \frac{\nabla^2\psi}{3}\right)A(e,p), \tag{2.15}$$

where $R_s = \sqrt{3}\sigma_1/\sigma_2$. Once ν and ξ are fixed, the values of e and p are realized following the probability distribution of Eq.(2.11), then the peak profile is expected to be well approximated by the typical profile given by Eq.(2.15) with the given parameters of (ν, ξ, e, p).

In this work, we consider a monochromatic power spectrum $\mathcal{P}_\zeta = \mathcal{A}_\zeta\delta(\ln(k/k_p))$ with $\mathcal{A}_\zeta = \sigma_0^2$, which is peaked at the scale k_p. The two-point correlation function is then given by $\psi(r) = \mathrm{sinc}(k_p r)$ with $\gamma = 1$ and $R_s = \sqrt{3}/k_p$ since $\sigma_n = \sigma_0 k_p^n$. Notice that, in the limit of $\gamma \to 1$, the conditional probability of ξ with a given value of ν is peaked precisely at $\xi = \gamma\nu = \nu$ as a Dirac delta function (see Eq. (7.5) in Ref. [26]). Therefore we can simply set $\xi = \nu$, and obtain

$$\bar{\zeta} = \zeta_{\mathrm{sp}} + \mu\frac{5A(e,p)}{2k_p^3 r^3}\left(3k_p r\cos(k_p r) + (r^2 k_p^2 - 3)\sin(k_p r)\right), \tag{2.16}$$

where $A(e,p)$ is given by Eq.(2.9) and $\zeta_{\mathrm{sp}} = \mu\,\mathrm{sinc}(k_p r)$ is the typical profile in spherical symmetry. Taking into account spherical coordinates, we can transform Eq.(2.9) into the Cartesian coordinates to obtain,

$$A(e,p) = \frac{3e}{r^2}(z^2 - y^2) + p\left[1 - 3\left(\frac{x}{r}\right)^2\right], \tag{2.17}$$
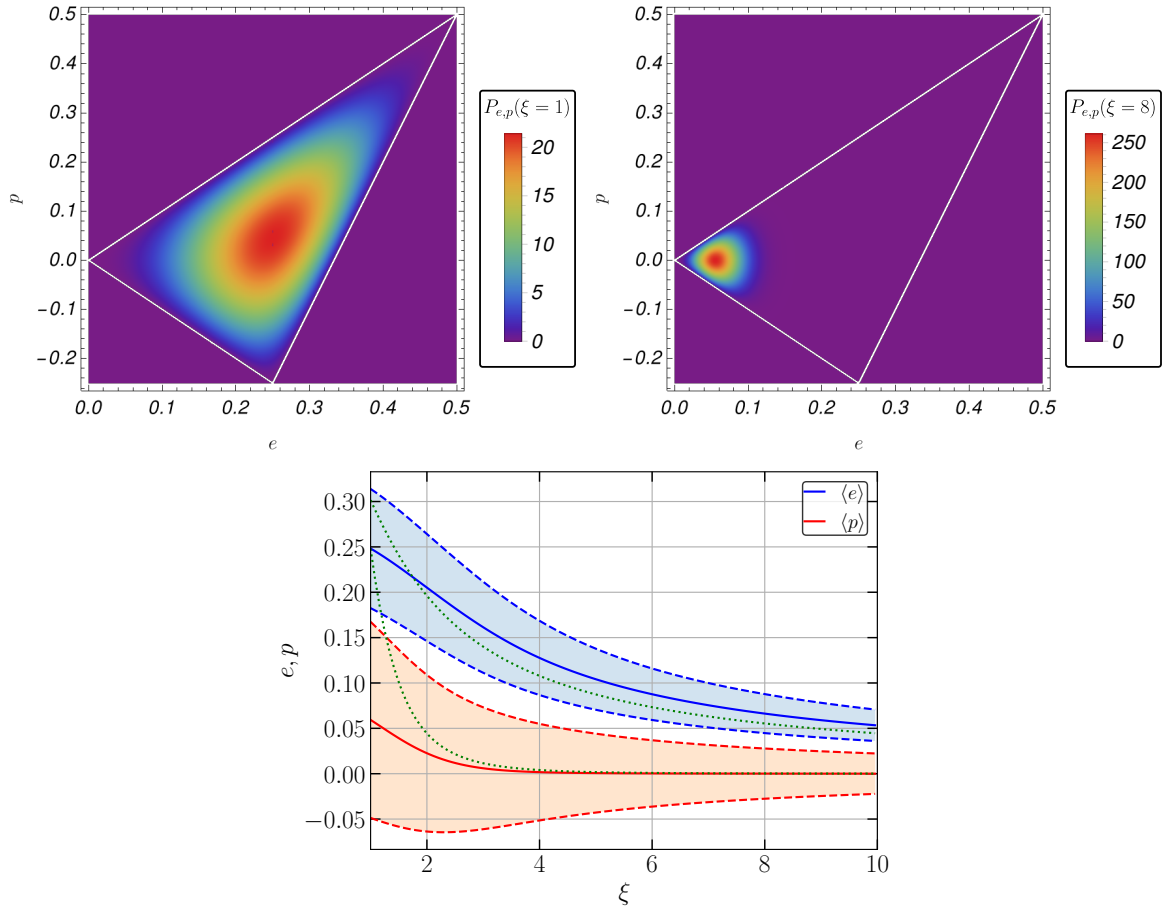
Figure 1. Top panels: Provability distribution of Eq.(2.11) in e and p for $\xi = 1$ (left panel) and $\xi = 8$ (right panel). Bottom panel: Mean values $\langle e \rangle$ and $\langle p \rangle$ of Eq.(A.1) and (A.2) (solid line) with one standard deviation (dashed line). The green dotted lines denote the mean values e_m and p_m in the large ξ limit given in Eq.(A.4) and (A.5).

which is practically more convenient for our numerical computation. Therefore, our initial condition for given values of (μ, e, p) is fixed by Eqs.(2.16) and (2.17). Although the dispersion of the profile around the typical one can be explicitly calculated as shown in Eq.(7.9) of [26] and in Eq.(2.10) of [67] for the case of the monochromatic spectrum, we do not consider the dispersion for simplicity. In Fig. 2, we show two examples of the initial curvature profile, assuming spherical symmetry with $e = p = 0$ and with $e = 0.1, p = 0.05$, which correspond to a triaxial oblate shape. It should be noted that, although the spatial profile given by Eqs.(2.16) and (2.17) is characterized by (μ, e, p), since the probability distribution for e and p is characterized by $\xi = \nu = \mu/\sigma_0$, the typical values of e and p depend on the value of the standard deviation σ_0 once the value of μ is fixed.

In Appendix B, we calculate the mass function of primordial black holes (PBHs) under the assumption of spherical symmetry with a monochromatic power spectrum and different w's. This calculation is later used to set a typical value for the fluctuation amplitude. We note that, the constraint from the total PBH fraction of dark matter $f_{\rm PBH}^{\rm tot} \leq 1$ requires that PBH formation is sufficiently rare, and the relevant amplitude of the peak is much larger than the standard deviation σ_0. That is, we need a high peak value, $\nu \gg 1$, which depends on
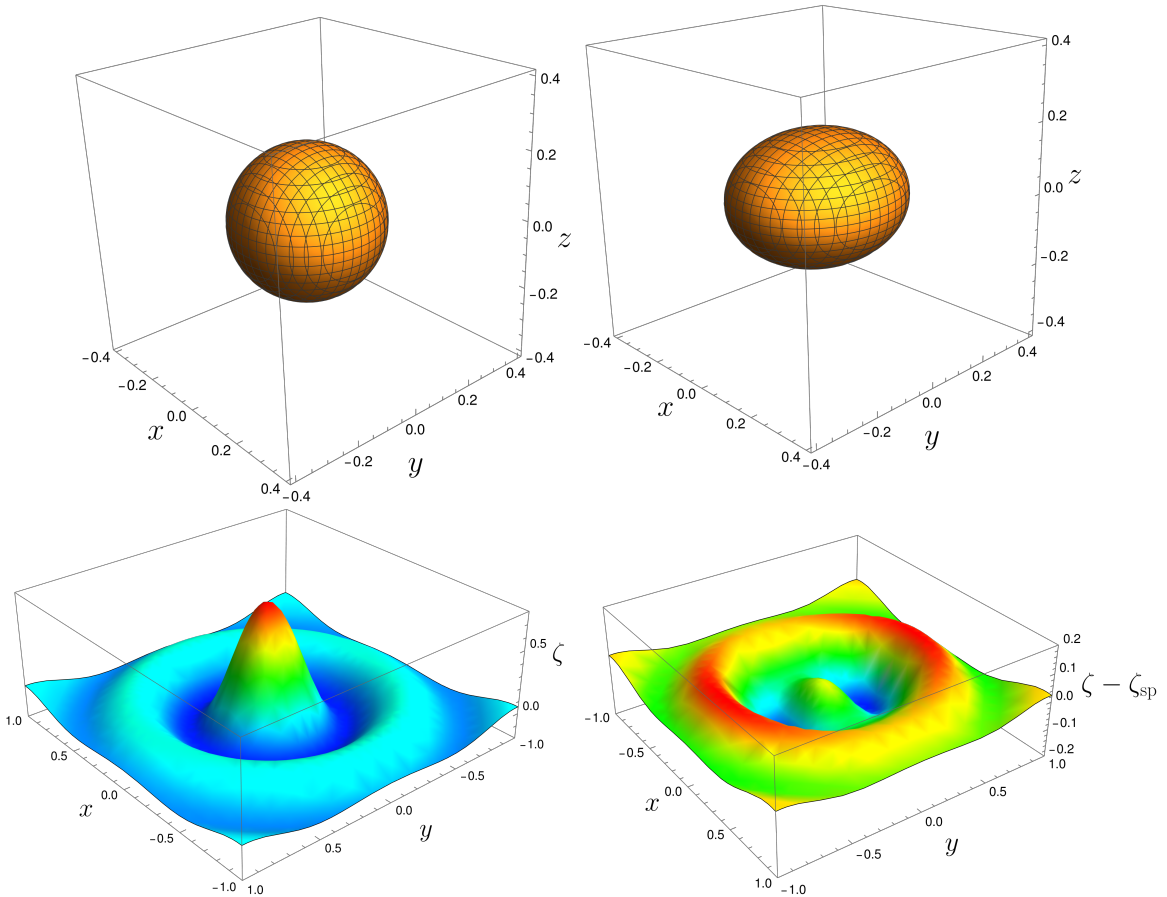
Figure 2. Top panels: Contour of ζ fixing $\zeta(x,y,z) = \mu/2$ with $\mu = 0.8$ for $e = p = 0$ (left panel) and $e = 0.1$ and $p = 0.05$ (right panel). Bottom panels: The left panel corresponds to a 3D plot of ζ in the plane $z = 0$ for $e = p = 0$, and the right panel is the difference in ζ between a spherical $\zeta_{\rm sp}$ configuration and non-spherical one with $e = 0.1$ and $p = 0.05$.

the mass scale where k_p is fixed (see Fig.15). The situation could differ for a broad spectrum, where $\gamma < 1$, but a large peak is still likely necessary.

3 Numerical method and procedure

We perform numerical simulations following the BSSN formalism [68, 69] decomposing the spacetime metric into the following 3+1 form:

$$ds^2 = -\alpha^2 dt^2 + \tilde{\psi}^4 \tilde{\gamma}_{ij}(dx^i + \beta^i dt)(dx^j + \beta^j dt), \tag{3.1}$$

where α is the lapse function, β^i is the shift-vector, $\tilde{\gamma}_{ij}$ is the conformal metric whose determinant is given by that of the flat reference metric, $\tilde{\psi}$ is the spatial conformal factor, which at super-horizon scales is $\tilde{\psi} = a^{1/2}\Psi = a^{1/2}\exp(-\zeta/2)$ with a being the scale factor of the FLRW background. All these variables are functions of t and $\vec{x}$. The time evolution of these variables at super-horizon scales has been analytically investigated in Ref. [70]. The energy momentum-tensor is given by the following perfect fluid form:

$$T_{\mu\nu} = (\rho + P)u_\mu u_\nu + P g_{\mu\nu}, \tag{3.2}$$

where u^μ, P, and ρ are the fluid 4-velocity, the pressure and the energy density, respectively. The equation of state is assumed to be the liner relationship $P = w\rho$ with a constant parameter w. For a later convenience, we define the fluid velocity relative to the Eulerian observer as

$$U^\mu = u^\mu/\Gamma - n^\mu, \tag{3.3}$$

where $n_\mu = -\alpha\partial_\mu t$ and Γ is the Lorentz factor defined by $\Gamma = -u^\mu n_\mu$. We use COSMOS code written in C++ [71, 72], which originally follows the SACRA code [73]. We basically use the same set-up and parameters (like the grid spacing, the CFL number condition and others) of the code used in [21] but modify the boundary conditions to handle only one quadrant in the simulations as in [18], taking into account the symmetry of our initial conditions, which makes the simulations less computationally expensive. First, we use the SPriBoSH code [74] to obtain efficiently the thresholds of PBH formation under the assumption of spherical symmetry (denoted by $\mu_{c,sp}$) for several values of w. In this work, we consider $w = 1/10$ and $1/3$ (soft and radiation cases), for what we obtain $\mu_{c,sp} \approx 0.3095$ and 0.6061, respectively (see Fig. 11 of Ref.[10] for other values of w). In the COSMOS code, we obtain the consistent values of $\mu_{c,sp}$ for the same spherical initial profile. This also helps us to determine the optimal number of grid points needed to achieve the desired accuracy in calculating the threshold values. We have found that setting $N = 60$ ($w = 1/10$) and $N = 100$ ($w = 1/3$) grid points in each direction gives enough accuracy for our purposes. We check the correctness of our simulations using the averaged Hamiltonian constraint violation and the maximum of that quantity, for which we show detailed examples in the appendix D.

Although the number of grid points is sufficient to follow the overall dynamics of the system, it is insufficient to precisely capture the apparent horizon formation without introducing the mesh-refinement procedure adopted in Ref. [21]. Instead of introducing the time-consuming mesh-refinement procedure, to determine whether a black hole forms or the fluid disperses in a FLRW background, we monitor the value of the lapse function at the origin. If the lapse function continuously decreases to a small value $\lesssim 0.1$, it suggests the eventual formation of an apparent horizon at sufficiently late times, indicating black hole formation. Conversely, if the lapse function exhibits a bouncing behaviour and increases after that, the fluid's mass excess disperses within the FLRW background, preventing black hole formation. A similar pattern is observed in the peak value of the energy density: a continuous increase signals black hole formation while reaching a maximum followed by a decline indicates fluid dispersion. This behaviour is quite universal, appearing in both spherically symmetric and non-spherical simulations, as noted in various studies [18, 74–78]. In some cases, our simulation failed with a significant violation of the Hamiltonian constraint at a late time. However, the behavior of the lapse function until the significant violation of the Hamiltonian constraint allows us to reliably infer whether the fluctuation will ultimately collapse to form an apparent horizon.

In the initial profile (2.16), we set $k_p = 10L$ and $H_0 := H(t_0) = 50L^{-1}$ with L being the coordinate length along each axis of the numerical domain given by $x \in [0, L]$, $y \in [0, L]$ and $z \in [0, L]$. The other initial quantities of the BSSN formalism are computed according to [18, 70]. The initial time corresponding to H_0 is given by $t_0 = \alpha_w/H_0$ with $\alpha_w = 2/(3w+3)$, and the initial energy density of the background universe is given by $\rho_b(t_0) = 3H_0^2/(8\pi)$. We also define the time of horizon crossing t_H of the mode k_p as $t_H = t_0(H_0/k_p)^{1/(1-\alpha_w)}$.

Practically, it is necessary to implement a window function in the curvature ζ to match the boundary condition $\Psi(r \to \infty) = 1$ at the last points of the grid. This is particularly relevant for the case of the sinc profile, which has small oscillations for a large radius. We

w	$k_p[\text{Mpc}^{-1}]$	$\mu_{c,sp}$	μ_t	$\sigma_0/10^{-2}$	ν_c
1/10	$10^{13.5}$	0.30948	0.313	3.524	8.781
1/10	10^7	0.30948	0.313	3.876	7.984
1/3	$10^{13.5}$	0.60613	0.6176	6.979	8.685
1/3	10^7	0.60613	0.6176	8.976	6.753

Table 1. Parameters μ_c, μ_t, σ_0, ν_c satisfying $f_{\text{PBH}}^{\text{tot}} \simeq 1$ for both cases of w with $k_p = 10^{13.5}\text{Mpc}^{-1}$ (asteroid mass range) and $k_p = 10^7\text{Mpc}^{-1}$ (solar mass range).

have found that the following functional form works well for our purposes:

$$W(r) = \exp\left\{ - \left(\frac{r - r_W}{\sigma_W} \right)^{\alpha_W} \right\} \tag{3.4}$$

with values $\sigma_W = 0.09L$, $r_W \approx 0.77L$ and $\alpha_W = 4$. Effectively, the window function will change the functional form of Eq.(2.16), but only for a large radius $r > r_W$. As found in [28], the threshold of formation is mainly affected by the shape around the radius at which the compaction function takes the maximum value.[3] This radius is much smaller than the radius where the window function is introduced. This expectation is confirmed in spherical symmetry by comparing the threshold with that obtained by the spherically symmetric code SPriBoSH without introducing the window function. The difference in the threshold values is within 0.01%. Although our case is now a simulation beyond spherical symmetry, we expect such consideration to also hold[4].

To investigate the impact of non-spherical configurations on the critical threshold values, we fix the value of $\mu > \mu_{c,sp}$, where $\mu_{c,sp}$ is the threshold value in spherical symmetry. We consider the mass spectrum derived with spherical symmetry to find a typical value μ_t. As is shown in AppendixB, the PBH mass function takes the maximum at a certain value of the mass. Since the mass is given as a function of the initial amplitude μ for the monochromatic spectrum[11, 82], we can find the value of μ for which the mass function takes the maximum. We use this value as a typical value of μ throughout this paper. For $\mu = \mu_t$, increasing the non-sphericity characterized by the two parameters e and p, we can find a boundary between black hole formation and dissipation. That is, we can divide the 2-dimensional parameter region of e and p into those two cases with the boundary curve described as $\mu_t = \mu_c(e, p)$, where $\mu_c(e, p)$ is the function of e and p which gives the threshold for a given set of e and p. The specific value of μ_t is given by 0.6176 for $w = 1/10$ and 0.313 for $w = 1/3$.

The dynamics of the system characterized by the parameter set (μ, e, p) is independent of the value of the standard deviation σ_0. However, once the value of μ is fixed, the probability distribution of e and p depends on σ_0. Since the PBH mass function also depends on σ_0, we fix the value of σ_0 by imposing $f_{\text{PBH}}^{\text{tot}} = 1$ for the spherically symmetric case. In Table 1, we summarize those parameters.

---

[3]The definition of the compaction function, which is defined for spherically symmetric fluctuations goes beyond the scope of the paper. We refer the reader to [79] for the original definition.

[4]The situation would differ for the behaviour of the PBH mass, where the shape of the profile beyond the maximum of the compaction function may have a significant effect [80, 81].

4   Numerical results

In this section, we present the main numerical results of our work. First, we show the dynamical evolution of the gravitational collapse for a few representative cases, and later, we focus on the threshold study in terms of the non-spherical parameters e and p.

4.1   Dynamical evolution of the non-spherical gravitational collapse

We analyze two specific cases to examine the dynamics of gravitational collapse. In the first case, the fluctuation exceeds the critical threshold ($\mu_{\rm t} > \mu_{\rm c}(e,p)$), leading to black hole formation. In the second case, the fluctuation remains below the threshold ($\mu_{\rm t} < \mu_{\rm c}(e,p)$), resulting in the dispersion of the fluctuation. To study the dynamical evolution of the fluctuation, we plot the ratio of $\rho/\rho_b(t)$ and the 4-velocity of the fluid U^i. We focus on the case of radiation-dominated Universe $w = 1/3$ and refer the reader to the appendix C for the $w = 1/10$ case. We found the qualitative behaviour to be the same for both $w = 1/3$ and $1/10$ except that the collapsing time is longer for $w = 1/10$, which is consistent with the case of spherical simulations [29].

Let's first consider a case where the fluctuation collapses into a black hole, in which the deviation from sphericity is not sufficiently large to avoid black hole formation. In particular, we choose $e = 0.08$ and $p = 0$, which correspond to the eigenvalues $\lambda_1/(\nu\sigma_2) = 1.24$, $\lambda_2/(\nu\sigma_2) = 1$, $\lambda_3/(\nu\sigma_2) = 0.76$ following Eq. (2.7). In Fig. 3, we show the evolution of the energy density ratio ρ/ρ_b for different times. One can see a characteristic ellipsoidal shape that changes over time. Initially, the shape of the energy density is shorter in the z-direction than x and y, since the length of fluctuation size in the i-axis goes like $\sim 1/\sqrt{\lambda_i}$, being λ_1 the largest eigenvalue (it should be noted that we follow the convention adopted in [26], $(1, 2, 3) \equiv (z, x, y)$ axes).

In Figs. 4 and 5, we plot the velocity U^x and U^z on the x-z plane, respectively, where we observe a highly non-spherical distribution. From the velocity plots of U^x and U^z, we observe that the collapse initially progresses slightly faster along the z-axis compared to the x-axis, as indicated by the higher collapse velocity in U^z (see the panels of $t/t_H \approx 0.04$). However, presumably because of the larger pressure gradient along the z-axis, the contraction along x-axis overtakes the contraction along z axis (see the panels of $t/t_H \approx 40.04$ and compare the values of U^x and U^z). Subsequently, the initial shape transitions from horizontally long to vertically long while preserving the ellipsoidal shape and reducing the size of the overdensity region (see the panels of $t/t_H = 90.04$ and those after that in Fig. 3). At very late times, the shape becomes nearly spherical.

In the velocity panels, we observe that, as the system approaches the formation of the apparent horizon at sufficiently late times, the fluid splits into two regions: one moving inward and the other moving outward, creating an under-dense region. This behaviour is typical in spherical relativistic simulations when the fluctuation amplitudes are near their critical threshold (see [74] for comparison).

Fig. 6 shows the the energy density, lapse function, and fluid velocity in the x components on the x-axis. Similar behaviors are found for y and z axes, and we do not display them. We observe a continuous decrease in the lapse function at the centre, and we infer the formation of an apparent horizon.

Let's now consider a case where the deviation from sphericity is sufficiently large, so that the fluctuation avoids black hole formation and disperses on the FLRW background. Specifically, we choose $e = 0.06$ and $p = 0.14$, which correspond to the eigenvalues $\lambda_1/(\nu\sigma_2) =$
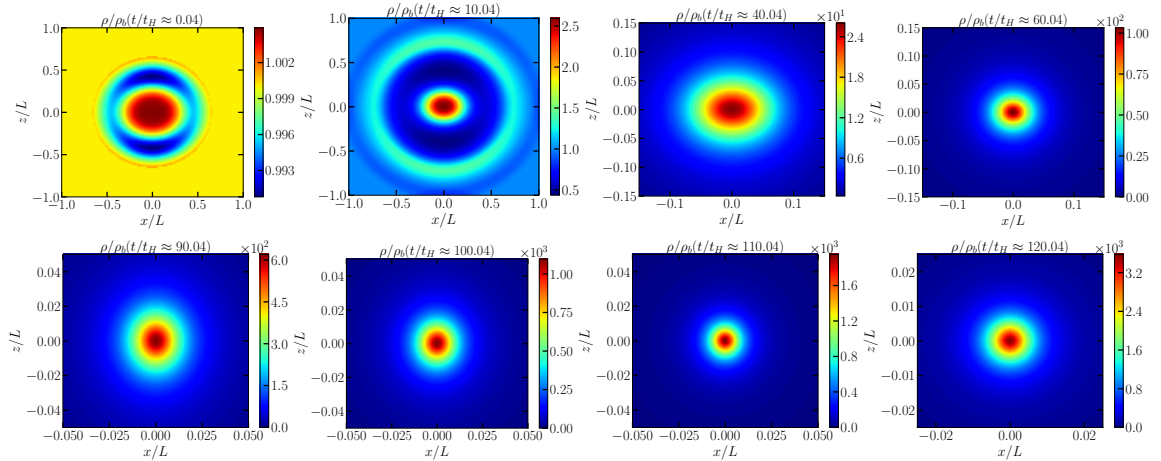
Figure 3. Snapshots of the evolution of ρ/ρ_b in the plane $y = 0$ for $e = 0.08$ and $p = 0$ with $w = 1/3$.
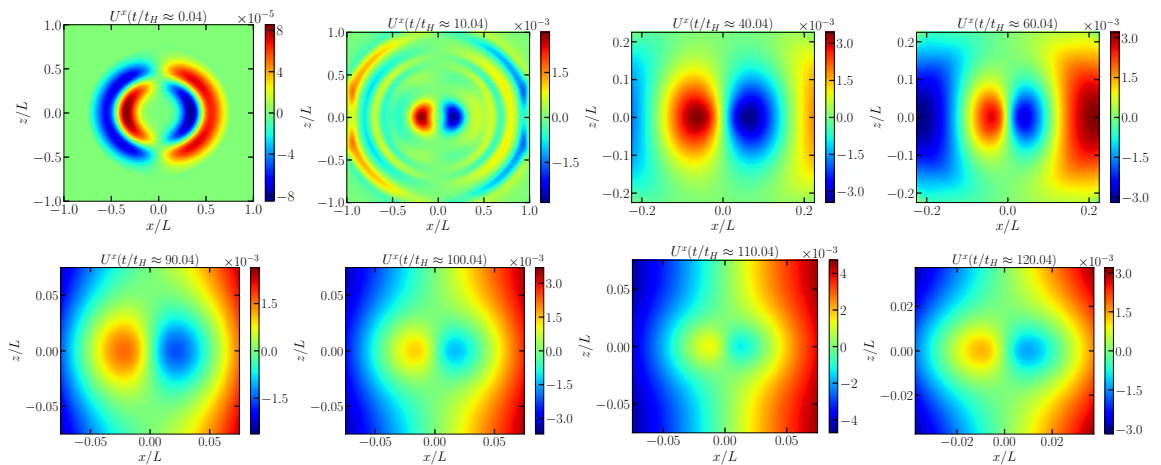

Figure 4. Snapshots of the evolution of the fluid velocity U^x in the plane $y = 0$ for $e = 0.08$ and $p = 0$ with $w = 1/3$.

1.32 , $\lambda_2/(\nu\sigma_2) = 0.72$ and $\lambda_3/(\nu\sigma_2) = 0.96$ following Eq.(2.7). In Figs. 7, 8 and 9, we show the evolution of the energy density ratio ρ/ρ_b and the velocities U^x and U^z for different times.

The initial shape is similar to the previous case, with horizontally long shape in the z-x plane due to the same ordering of eigenvalues $\lambda_1 > \lambda_2 > \lambda_3$. We observe a similar behaviour regarding oscillatory behavior of the ellipsoidal shape with a tendency to remain spherical at very late times. Compared to the previous case, the peak value of the energy density reaches a maximum before subsequently decreasing. The velocities, U^x and U^z, indicate an early-time contraction of the fluid's overdense region. However, at later times, no rarefaction waves are observed; instead, the fluid is simply dispersed within the region surrounding the fluctuation. In Fig. 10, we plot the variables on the x-axis as in the previous case. Notably, we observe that the lapse function at the centre experiences a bouncing behaviour as expected, indicating that the fluctuation will not form an apparent horizon.

Finally, Fig. 11 shows the time evolution of the lapse function at the centre $\alpha(\vec{r} = 0)$ for different configurations. The figure highlights the detailed bouncing behaviour of the lapse
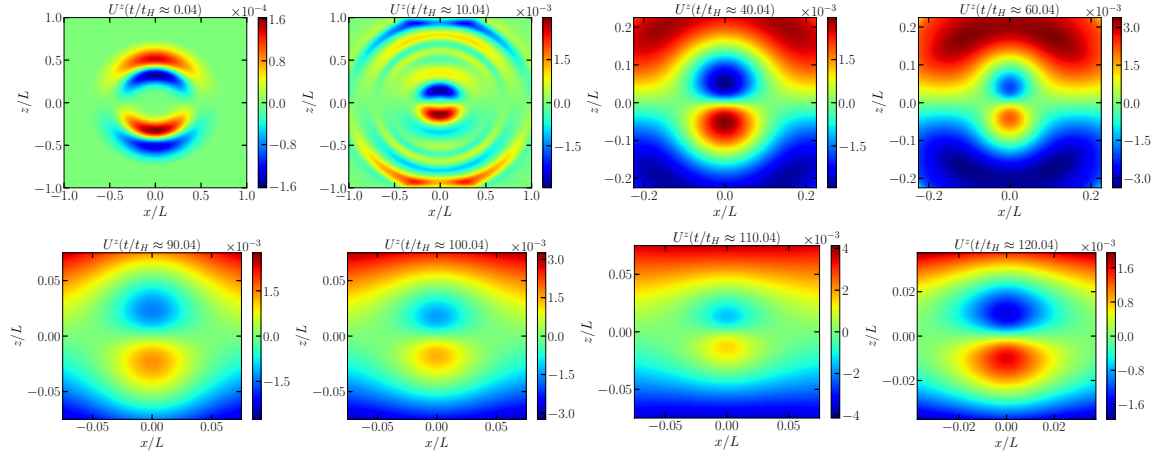
Figure 5. Snapshots of the evolution of the fluid velocity U^z in the plane $y = 0$ for $e = 0.08$ and $p = 0$ with $w = 1/3$.
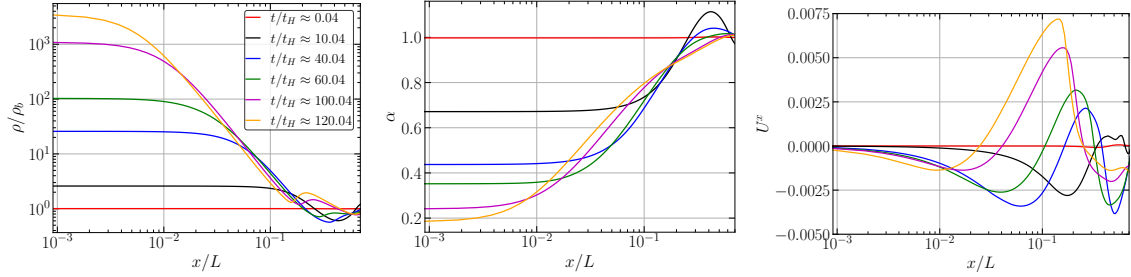

Figure 6. Snapshots of the energy density ρ/ρ_b (left-panel), lapse function α (middle-panel) and Eulerian velocity U^x (right-panel) on the x axis ($y = z = 0$) for $e = 0.08$ and $p = 0$.
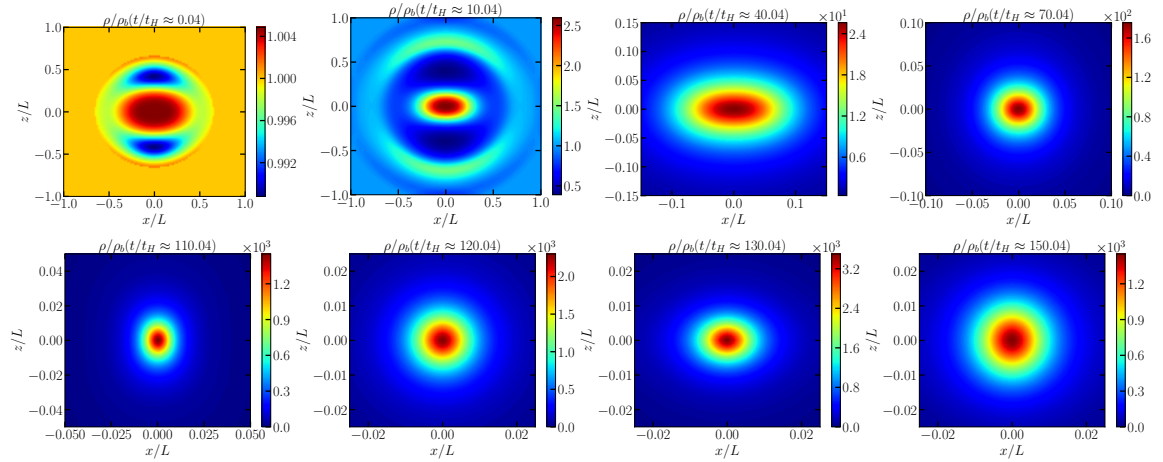

Figure 7. Snapshots of the evolution of ρ/ρ_b in the plane $y = 0$ for $e = 0.06$ and $p = 0.14$ with $w = 1/3$.

function, which indicates apparent horizon formation when $\alpha(\vec{r} = 0)$ continuously decreases and approaches to zero. We can observe that the time scale of the gravitational collapse
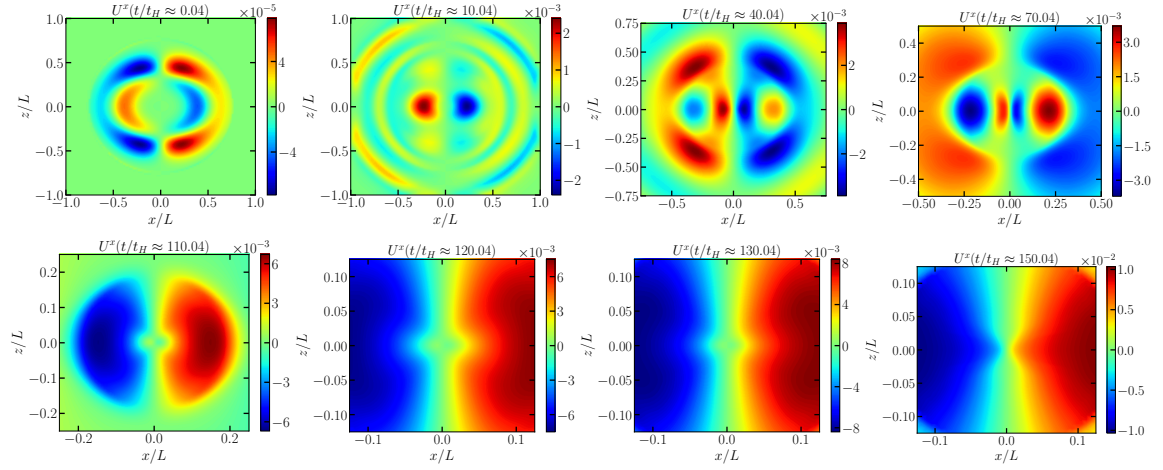
Figure 8. Snapshots of the evolution of the fluid velocity U^x in the plane $y = 0$ for $e = 0.06$ and $p = 0.14$ with $w = 1/3$.
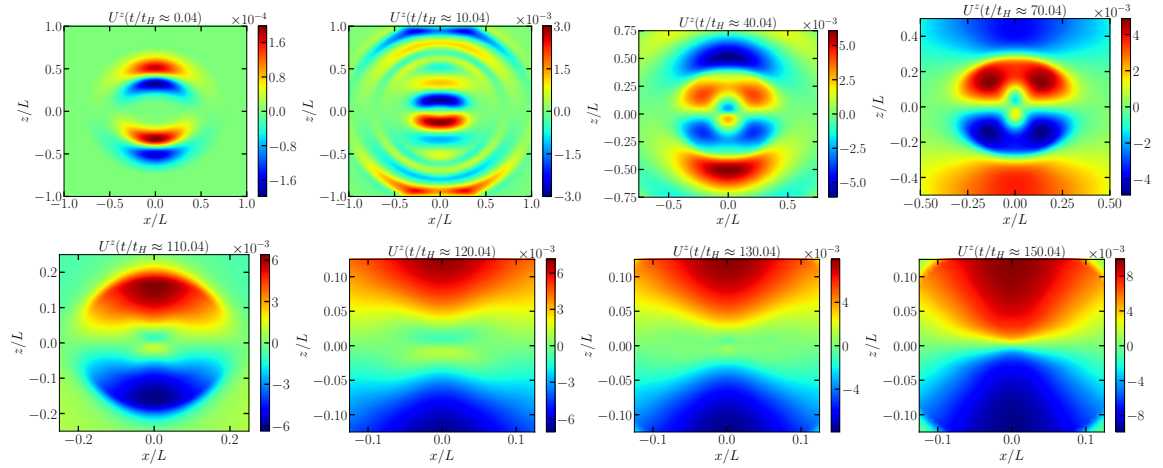

Figure 9. Snapshots of the evolution of the fluid velocity U^z in the plane $y = 0$ for $e = 0.06$ and $p = 0.14$ with $w = 1/3$.
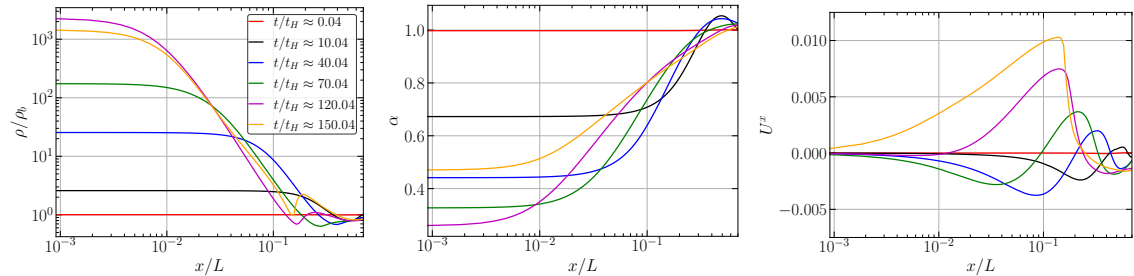

Figure 10. Snapshots of the energy density ρ/ρ_b (left-panel), lapse function α (middle-panel) and Eulerian velocity U^x (right-panel) on the x axis ($y = z = 0$) for $e = 0.06$ and $p = 0.14$.

is longer for a softer equation of state (smaller w). The top panels display cases with the fixed amplitude μ_{t}. Generally, we observe that non-spherical effects ($e, p \neq 0$) tend to slow down the collapse and can significantly increase the collapse time. The bottom panels show different configurations with varying amplitudes μ while fixing $p = 0$. Here, we find that as μ increases beyond the critical value for spherical collapse, the deviation from sphericity required to prevent collapse also becomes larger, showing that non-spherical effects tend to prevent black hole formation. By running multiple simulations and analyzing the bouncing behaviour of the lapse function, we identified the threshold values, which will be discussed in detail in the next section.
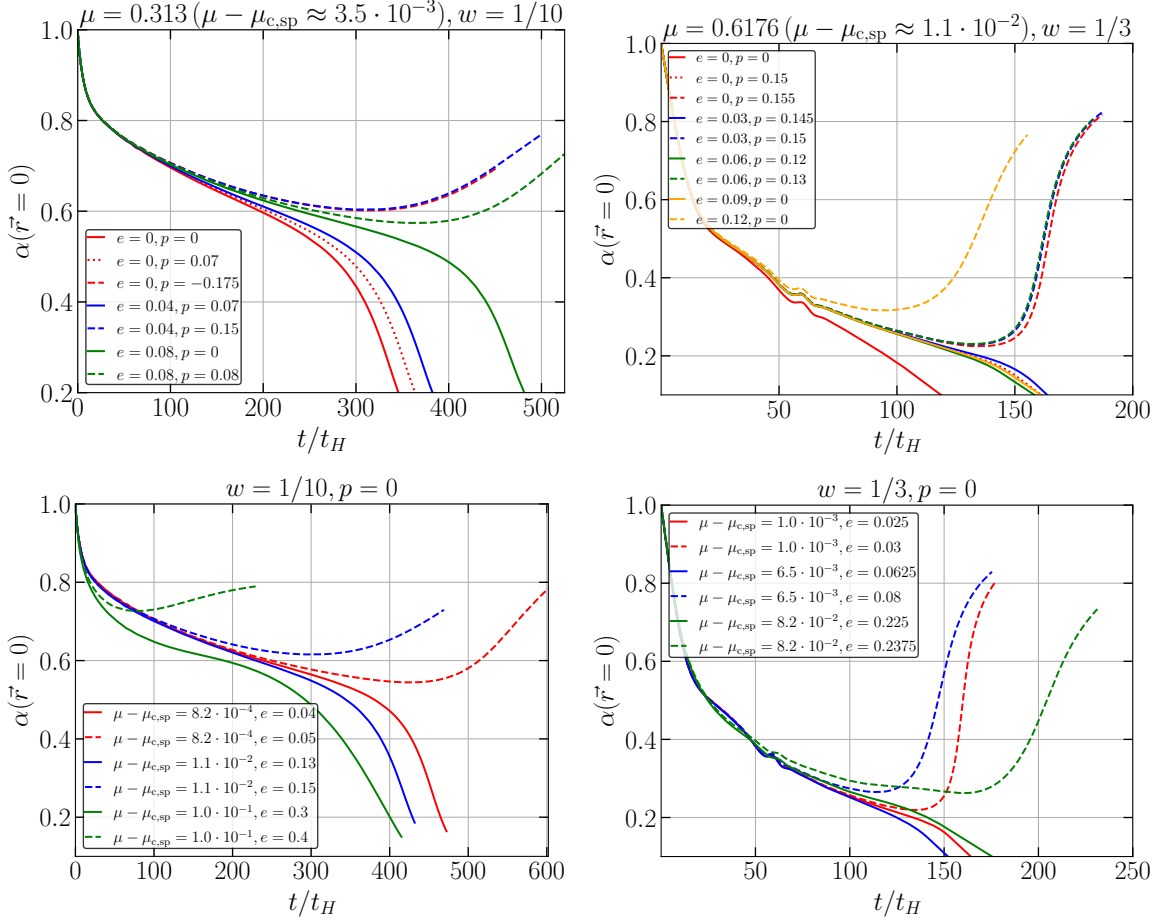

Figure 11. Top-panels: Evolution of the lapse function at the origin for different configurations characterized by different values of e and p for $w = 1/10$ with $\mu = 0.313$ (left-panel) and $w = 1/3$ with $\mu = 0.6176$ (right-panel). Bottom-panels: The same as the top-panel, but with $p = 0$ for different values of e and the amplitudes $\mu - \mu_{\mathrm{c,sp}}$.

One remarkable behavior observed in this section from the non-spherical configuration is the damping oscillatory behaviour of the ellipticity. This suggests that the non-sphericity in our models decays over time, and remains small. This observation is consistent with findings from non-spherical simulations (small deviations from sphericity) in asymptotically flat spacetimes [22, 83]. More complex dynamics could arise with larger deviations from sphericity (see, for instance, [84]) or with a misaligned deformation tensor, as seen in [21].

4.2 Non-sphericity dependence of the thresholds with the typical amplitude $\mu_{\rm t}$.

We now investigate the threshold for black hole formation in terms of the non-spherical parameters e and p. We begin by fixing the amplitude μ, to the typical value $\mu_{\rm t}$ used in the previous section for both cases of $w = 1/10$ and $w = 1/3$. With μ fixed, we perform a series of simulations to determine the critical values of e and p at which a fluctuation will either collapse to form a black hole or disperse. From these simulations, we identify the critical configurations, denoted as $(\mu_{\rm t}, e, p = \tilde{p}_{\rm c}(e))$, where we describe $\tilde{p}_c$ as a function of e because the critical configurations draw a line in the space of e and p. The results are presented in Fig. 12, where green and red dots indicate cases of black hole formation and dispersion, respectively. The threshold is estimated as the midpoint between these cases. The magenta and orange lines smoothly connect these points delineating the critical line in the (e, p) parameter space for the cases with $w = 1/10$ and $w = 1/3$, respectively. Configurations inside these dashed lines will lead to black hole formation, as the deviations from sphericity are not large enough to prevent collapse. In contrast, configurations outside this region have sufficiently large deviations from sphericity, preventing the fluctuations from collapsing.

We find that, from our numerical results, the critical line described by $p = \tilde{p}_{\rm c}(e)$ closely follow a *superellipse* expressed as

$$\left(\frac{\tilde{p}_{\rm c}^\pm(e)}{p_0^\pm}\right)^{n^\pm} + \left(\frac{e}{e_0}\right)^{n^\pm} = 1 \Rightarrow \tilde{p}_{\rm c}^\pm(e) = \pm p_0^\pm \left[1 - \left(\frac{e}{e_0}\right)^{n^\pm}\right]^{1/n^\pm}, \tag{4.1}$$

where $\tilde{p}_{\rm c}^\pm(e)$ is defined such that the critical line is given by $p = \tilde{p}_{\rm c}(e) = \tilde{p}_{\rm c}^\pm(e)$ for $p \gtrless 0$, and $e_0, p_0^\pm$ and the exponent $n^\pm$ are the parameters characterising the superellipse. Making a non-linear fit of Eq. (4.1) with our numerical results, we obtain $n^+ \approx 2.44 \pm 0.03$, $n^- \approx 1.70 \pm 0.02$ for $w = 1/3$ and $n^+ \approx 2.53 \pm 0.10$, $n^- \approx 1.70 \pm 0.05$ for $w = 1/10$. The behaviour of $\tilde{p}_{\rm c}(e)$ is not symmetric for the reflection along e axis, that is, $\tilde{p}_{\rm c}^+(e) \neq -\tilde{p}_{\rm c}^-(e)$. This is expected since the set of eigenvalues λ_l is not the same when considering $p \to -p$ with a fixed e. For the cases $e = 0$, we found $\tilde{p}_{\rm c}^+(0) = p_0^+ < |\tilde{p}_{\rm c}^-(0)| = |p_0^-|$ indicating that a slightly larger deviation from sphericity is required for the fluctuations to collapse for prolate cases ($p < 0$) compared with oblate cases ($p > 0$). Note that the value of $\tilde{p}_{\rm c}(e)$ does not change much in the region where the probability given by Eq. (2.11) is non-zero. This supports the idea that we can ignore the p dependence in the threshold estimation when we estimate the PBH mass function.

Interestingly, we do not observe significant differences in the functional form of the critical line $p = \tilde{p}_{\rm c}(e)$ for the two values of w considered. This suggests that the functional form of Eq. (4.1) might have some "universality" with similar values of $n^\pm$, indicating that the threshold of collapse is determined by the initial ellipticity irrespective of the parameter w of the equation of state. However, simulations with other profiles and $\mu - \mu_{\rm c,sp}$ values would be needed to clarify the validity of this hypothesis.

4.3 Critical ellipticity as a function of the initial amplitude μ

Here, let us focus on the cases with $p = 0$ having the weak p-dependence of the threshold value in the parameter region relevant to the PBH mass function revealed in the previous section. Then, for a fixed value of $\mu > \mu_{\rm c,sp}$, we can find the critical value $e_{\rm c} = \tilde{e}_{\rm c}(\mu)$ as the threshold of e for black hole formation. We describe this critical value as $\tilde{e}_{\rm c}(\mu)$ since it depends on the value of μ. We conduct new simulations to find $\tilde{e}_{\rm c}(\mu)$ for $w = 1/3$ and
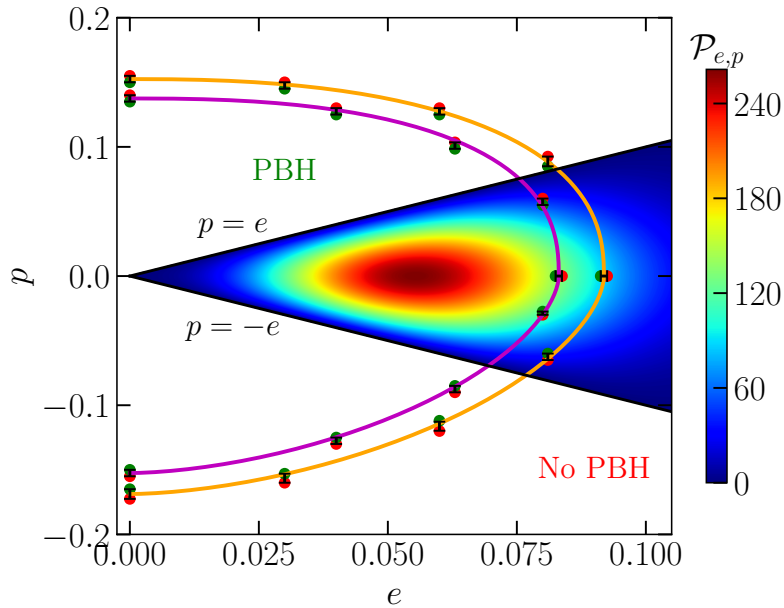
Figure 12. "Phase diagram" in the (e, p) plane for the typical initial amplitude $\mu = \mu_t$. The red and green dots denote configurations of e and p that avoid and form black holes, respectively. The magenta and orange lines represent the numerical fitting of Eq.(4.1) to the numerical threshold values (infer as the middle point between the green and red points) for the case $w = 1/10$ and $w = 1/3$, respectively. The coloured region corresponds to the probability distribution $\mathcal{P}_{e,p}$ (Eq.(2.11)) fixing $\nu_c = 8$.

$w = 1/10$. In Fig. 13, we present the results of our simulations. Our numerical results closely follow a power-law behavior, described by:

$$\tilde{e}_{\rm c}(\mu) = \mathcal{K}_e \left(\frac{\mu - \mu_{\rm c,sp}}{\mu_{\rm c,sp}} \right)^{\gamma_e}, \tag{4.2}$$

in the range $10^{-3} \lesssim (\mu - \mu_{\rm c,sp})/\mu_{\rm c,sp} \lesssim 10^0$. The values of the exponent γ_e and the constant $\mathcal{K}_e$ are given by $\mathcal{K}_e \approx 0.53$ and $\gamma_e \approx 0.41$ for $w = 1/10$, and $\mathcal{K}_e \approx 0.56$ and $\gamma_e \approx 0.45$ for $w = 1/3$.

Our numerical results have been done in the range $10^{-3} \lesssim (\mu - \mu_{\rm c,sp})/\mu_{\rm c,sp} \lesssim 10^0$. Extending the analysis to smaller values would require significantly more computational time and higher resolution, which we leave for future research. However, in the small $\mu - \mu_{\rm c,sp}$ limit, the threshold configuration satisfying $e_{\rm c} = \tilde{e}_{\rm c}(\mu)$ approaches the spherically symmetric critical solution. Therefore, if the power law behavior is totally characterized by the spherical critical solution and perturbation modes around that, the behavior is preserved for $(\mu - \mu_{\rm c,sp})/\mu_{\rm c,sp} \ll 10^{-3}$. This expectation, though, would need to be confirmed through detailed analyses.

Taking into account Eqs.(4.2) and (4.1), we could incorporate the behaviour of $\tilde{e}_{\rm c}(\mu)$ into $\tilde{p}_{\rm c}(e)$. That is, for instance, assuming the exponent $n_\pm$ is unchanged, we may extend the parameters $p_0^\pm$ and e_0 as functions of μ written as $\tilde{p}_0^\pm(\mu) = \tilde{p}_0^\pm(\mu_t) \times \tilde{e}_c(\mu)/\tilde{e}_c(\mu_t)$ and $\tilde{e}_0(\mu) = \tilde{e}_c(\mu)$. Then we can draw contours in the e-p plane. For a smaller value of μ, the size of the contour shrinks toward the origin (spherical case) and vanishes in the limit $\mu \to \mu_{\rm c,sp}$. However, this proposal requires further validation through additional simulations,
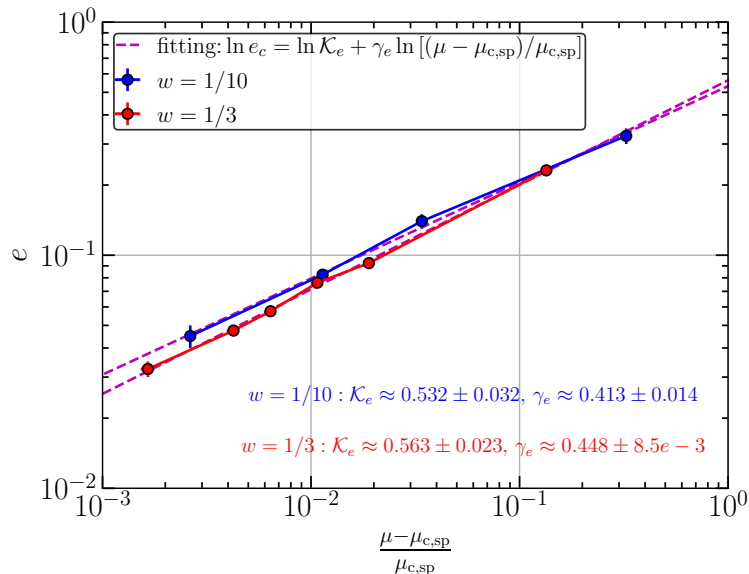
Figure 13. The critical value e_c with $p = 0$ is depicted as a function of $(\mu - \mu_{c,sp})/\mu_{c,sp}$ together with the error bars given by the intervals between the parameter values of e for the corresponding two cases of the black hole formation and dissipation. The dashed magenta lines correspond to the fitting to the equation $\tilde{e}_c(\mu) = \mathcal{K}_e[(\mu - \mu_{c,sp})/\mu_{c,sp}]^{\gamma_e}$, whose values $\mathcal{K}_e$ and γ_e are shown in the plot for the case $w = 1/10$ (blue) and $w = 1/3$ (red).

particularly those examining a wider range of profiles. This is an avenue left for future research.

Our numerical results in Fig. 13 demonstrate that non-spherical effects make the gravitational collapse of fluctuations harder compared to the spherical case. Moreover, due to the behaviour of Eq.(4.2), even a slight deviation from sphericity can prevent a fluctuation from collapsing into a black hole if those fluctuations have an amplitude near the threshold in the critical regime. Let us evaluate, due to the nonspherical effects, how large fraction is excluded from the total number of black holes which is supposed to be formed without taking into account the non-sphericity. The remaining fraction can be estimated by integrating the probability distribution of e and p in the region enclosed by $p = \pm e$ and $p = \tilde{p}_c(e)$ with a fixed value of μ. For simplicity, we approximate the line $p = \tilde{p}_c(e)$ by $e = \tilde{e}_c(\mu)$ of a vertical line in e-p plane and integrate the probability distribution $\mathcal{P}_{e,p}$ over the region $\mathcal{R}$ defined by

$$\mathcal{R}(\mu) \in \{0 \leq e \leq \tilde{e}_c(\mu) , \, -\tilde{e}_c(\mu) \leq p \leq \tilde{e}_c(\mu)\} \tag{4.3}$$

in the parameter space (e, p). Note that this approach provides an upper bound for the estimation. As shown in Fig. 12, although there are regions with $p > \tilde{p}_c^+(e)$ or $p < \tilde{p}_c^-(e)$ inside $\mathcal{R}$, which cause an overestimation of the number of black holes, the effects are negligible for a typical value of μ.

The integration of the probability distribution with the fitting function (4.2) can be found in Fig. 14 in percentage "%". For a typical value of μ, which gives $(\mu - \mu_{c,sp})/\mu_{c,sp} \sim 1\%$, about 90% of the configurations will collapse depending on w and ν chosen, overcoming the non-spherical effects. This supports the conclusion reached in [18] for $w = 1/3$ with an exponential Gaussian profile considering $p = \pm e$, which found that non-spherical effects do

not significantly impact the threshold by more than $\sim 1\%$[5]. Our findings suggest that the total number of black holes can be accurately estimated based on the threshold given by spherically symmetric simulations for typical settings.

On the other hand, if we focus on the critical scaling regime, in which the amplitude is very close to $\mu_{\rm c,sp}$, the number of configurations collapsing into black holes can be significantly reduced. For instance, for $(\mu - \mu_{\rm c,sp})/\mu_{\rm c,sp} = 10^{-3}$, most of the configurations are prevented from collapsing into black holes although it slightly depends on w and ν. Therefore the non-spherical effects can be highly significant in the critical regime, preventing a large fraction of configurations from collapsing into black holes. Nevertheless, we report in the accompanying letter [85] that, in terms of the PBH mass function, the effects of the ellipticity may not have a significant impact even on the power-law small mass tail originates from the critical behavior.
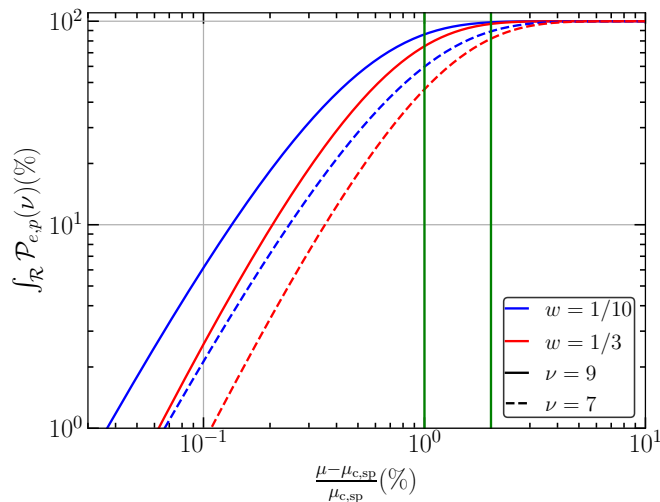

Figure 14. Integration of the probability distribution of Eq. (2.11) integrated over the domain $\mathcal{R}$ defined in Eq.(4.3) in terms of $(\mu - \mu_{\rm c,sp})/\mu_{\rm c,sp}$ in percentatge value %. Red and blue lines correspond to the cases with radiation and soft equations of state, respectively. The solid and dashed lines correspond to the cases for $\nu = 9$ and $\nu = 7$, respectively, which corresponds to putting the scale k_p at different mass-scales; see Table1 and appendix B for details. The two green vertical lines indicate 1% and 2% respectively.

We also conclude that non-spherical effects in a moderately soft equation of state ($w = 1/10$) do not play a significant role. This finding contrasts with the expectations in the literature, where non-spherical effects were anticipated to have a more substantial impact in soft equations of state compared to radiation-dominated scenarios. One of the reasons for this result is the following. In general, the nearly spherical configuration is guaranteed by the validity of the high peak approximation $\nu \gg 1$. For the soft equation of state, since the pressure gradient effects are weaker, typically expected non-sphericity is larger than the case of the radiation fluid case for a fixed value of the bare amplitude μ, and we naively expect the non-spherical effects to be more substantial for soft equations of state. However, because we fix the value of σ_0 to have $f_{\rm PBH}^{\rm tot} \simeq 1$, the threshold value of $\nu = \mu/\sigma_0$, which is relevant

---

[5]Notice that, in [18], differently from this paper, another probability distribution, which is defined without considering the real space number density, is used for simplicity because this simplification does not cause any qualitative difference.

for the high peak approximation, is not significantly different from the case with $w = 1/3$ (see Table1). Then the spherically symmetric assumption also works for the soft equation of state with $w = 1/10$.

The fact that we do not observe a significant impact of non-spherical effects on gravitational collapse for $w = 1/10$ compared to $w = 1/3$ (as shown in Fig. 13) could be attributed to the following reason. First, we should note that the collapsing dynamics of the ellipsoidal system is different from the dust case and the well-known instability shown by Lin-Mestel-Shu [86] does not apply. Here let us try to understand our results following the Jeans criterion, which states that the system is unstable against gravitational collapse if the free-fall time scale is shorter than the sound wave crossing time scale. In our setting, at least for a relatively small ellipticity, the free-fall time scale $\sim 1/\sqrt{\rho}$ would be still relevant, and it does not change much due to the small ellipticity e because the product $\lambda_1 \lambda_2 \lambda_3$ is conserved at the linear order of e with $p = 0$. On the other hand, the sound wave crossing time scale is expected to be shorter because the sound wave along the short axis may propagate through the system in a shorter time. Therefore the gravitational collapse is expected to be harder. Although, with a given value of the initial amplitude μ, this effect is expected to be more pronounced for larger w, the relative effect may be comparable since the threshold amplitude is smaller for a smaller value of w.

Once non-spherical effects become dominant impeding factors against the gravitational collapse as $w \to 0$, the Jeans criterion does not apply, and we need to consider different criteria. Non-sphericities are expected to grow during collapse [86, 87]. This could lead to complex dynamics associated with the deformation [88] and rotation of over-densities [32], and velocity dispersion potentially play a significant role [89]. Further investigation is needed to clarify this aspect.

5   Conclusions

In this work, we employed $3 + 1$ relativistic numerical simulations to study the collapse of super-horizon curvature fluctuations with an ellipsoidal geometry, characterized by ellipticity (e) and prolateness (p), in line with peak theory [26] assuming a monochromatic power spectrum. When analyzing the dynamics for the two cases of the equation of state with $w = 1/10$ and $1/3$, we observe a characteristic behaviour of the oscillating ellipsoidal shape between oblate and prolate configurations. This oscillation persists until very late times, when the shape becomes nearly spherical, just before the formation of the apparent horizon. Although this implies that the assumption of an exactly spherical shape is not valid until the final stages of collapse, our results indicate that, for the cases tested, the non-sphericity decays over time, in agreement with [22, 83], with relatively small non-sphericities in the initial data. On the other hand, non-spherical collapse will be accompanied by the emission of gravitational waves [90]; however, a thorough investigation of this phenomenon is left for future research.

We have also examined how the threshold for black hole formation depends on the parameters e and p. When we fixed the amplitude as a typical value μ_t, we found that the curve $p = p_c(e)$ which describes the boundary of the region of black hole formation on the e-p plane fits well a superellipse curve (described by Eq.(4.1)) characterized by an exponent $n^\pm$, where the sign $\pm$ denotes the two branches for the region $p \gtrless 0$. It would be interesting to investigate that functional form in terms of μ, and its profile dependence for developing

an analytical framework similar to spherically symmetric cases [28, 29] or including non-Gaussianities [67].

In addition, we have shown that non-spherical effects can be highly significant for fluctuations with amplitudes very close to their threshold, $\mu_{\rm c}$, where even small deviations from sphericity can prevent black hole formation. This implies that, even for large peaks ($\nu \gg 1$), a substantial fraction of the configurations described by Eq.(2.11) can avoid black hole formation, as illustrated in Fig.14. However, when considering the probability distribution of these peaks, we find that around 90% of the non-spherical configurations cause only a small shift in the threshold, $(\mu - \mu_{\rm c,sp})/\mu_{\rm c,sp}$, of less than 2%. This suggests that most configurations are unaffected by the small threshold shift. This conclusion aligns with the findings of [18] for a radiation-dominated Universe. Given that our study uses a different curvature profile from [18], it may indicate that this conclusion could hold for other curvature profiles as well. However, a detailed study examining profile dependence is needed to clarify the significance of the non-spherical effects.

Finally, when comparing our results for a radiation-dominated universe to those for a softer equation of state, we do not observe significant differences. This suggests that non-spherical effects are not much more pronounced for a moderately soft equation of state compared to a radiation fluid, contrary to some expectations in the literature. It is likely that non-spherical effects only become dominant in the almost pressureless systems in which the non-spherical effects are dominant impeding factors against gravitational collapse. Therefore, we conclude that for a moderately soft equation of state (such as the cases $w \geq 1/10$ we tested), non-spherical effects do not significantly alter the threshold for black hole formation compared to the radiation case, $w = 1/3$. This implies that the results from spherical simulations should provide a sufficiently accurate threshold value for black hole formation for practical use. Our numerical results have been used in our companion *letter* [85], showing that, non-spherical configurations do not have a significant impact on the PBH mass function although they become highly significant in the critical regime in terms of the probability distribution of the initial amplitude (see Fig.14).

A Analytical formulas for the mean values of e and p

The mean values of e and p for the probability distribution of Eq.(2.11) are given by

$$\langle e \rangle(\xi) = \frac{3 \exp\{-5\xi^2/2\}}{200\sqrt{10\pi}\,\xi\,f(\xi)}\left[\exp\left\{\frac{15\xi^2}{8}\right\}\left(\sqrt{30\pi}\,(15\xi^2+4)\,\mathrm{erf}\left(\frac{1}{2}\sqrt{\frac{15}{2}}\xi\right) + 45\xi\,(5\xi^2+12)\right)\right.$$
$$\left. + 4\exp\left\{\frac{5\xi^2}{2}\right\}\left(3\sqrt{10\pi}\left(\mathrm{erf}\left(\sqrt{\frac{5}{2}}\xi\right) - \mathrm{erf}\left(\frac{1}{2}\sqrt{\frac{5}{2}}\xi\right)\right) + 50\xi^3 - 180\xi\right) + 60\xi\right], \tag{A.1}$$

$$\langle p \rangle(\xi) = \frac{9 \exp\{-5\xi^2/2\}}{200\sqrt{10\pi}\,\xi\,f(\xi)}\left[4\sqrt{10\pi}\exp\left\{\frac{5\xi^2}{2}\right\}\left(\mathrm{erf}\left(\frac{1}{2}\sqrt{\frac{5}{2}}\xi\right) + \mathrm{erf}\left(\sqrt{\frac{5}{2}}\xi\right)\right)\right. \tag{A.2}$$
$$\left. + \exp\left\{\frac{15\xi^2}{8}\right\}\left(\sqrt{30\pi}\,(15\xi^2+4)\,\mathrm{erf}\left(\frac{1}{2}\sqrt{\frac{15}{2}}\xi\right) - 15\xi\,(5\xi^2+12)\right) + 60\xi\right].$$

In the large ξ limit, the probability distribution Eq.(2.11) can be indeed approximated by a Gaussian and takes the simpler form:

$$P_{\rm ep}(e,p) \approx P_{\rm e,p} \exp\left[-\frac{(e-e_m)^2}{2\sigma_e^2} - \frac{(p-p_m)^2}{2\sigma_p^2}\right], \tag{A.3}$$

where the mean values e_m and p_m and dispersions σ_e and σ_p are given by

$$e_m = \frac{1}{\sqrt{5}\xi\sqrt{1+6/(5\xi^2)}}, \quad \sigma_e = \frac{e_m}{\sqrt{6}}, \tag{A.4}$$

$$p_m = \frac{1}{\sqrt{5}\xi^4[1+6/(5\xi^2)]^2}, \quad \sigma_p = \frac{e_m}{\sqrt{3}}. \tag{A.5}$$

B   High peaks for PBH formation assuming spherical symmetry

In this appendix, under the assumption of spherical symmetry, we quantify the height of the peaks $\nu_{\rm c}$ fixing the ratio of PBHs in dark matter $f_{\rm PBH}^{\rm tot}$. We consider the case of a monochromatic power spectrum $\mathcal{P}_\zeta = \mathcal{A}_\zeta \delta(\ln(k/k_p))$ as in section 2. To statistically compute the abundance of peaks leading to black hole formation, we follow the approach of [91, 92] based on the Gaussian statistics of ζ (see also [65] where the approach was also used in the context of the PTA analysis with arbitrary w).

The typical profile for the monochromatic power spectrum (which is equivalent to the mean profile for that particular case) is given by

$$\zeta_{\rm sp} = \mu \, {\rm sinc}(k_p r). \tag{B.1}$$

Notice that for that case, the statistical procedure is simplified since only one relevant scale is involucrated, given by k_p. The normalized height of the peak is then given by $\nu = \mu/\sqrt{\mathcal{A}_\zeta}$. The number of peaks in terms of ν is computed as,

$$n_{\rm pk}(\nu) = \frac{1}{(2\pi)^2} \frac{1}{3^{3/2}} k_p^3 f(\nu) \frac{1}{\sqrt{\mathcal{A}_\zeta}} e^{-\frac{1}{2}\nu^2}, \tag{B.2}$$

where $f(\nu)$ is the function introduced in Eq.(2.12). For the monochromatic spectrum, the number density of PBHs $n_{\rm PBH}(M)$ for a fixed mass M is simply given by [6]

$$n_{\rm PBH}(M)d\ln M = n_{\rm pk}(\nu)\left|\frac{d\ln M}{d\mu}\right|^{-1} d\ln M, \tag{B.3}$$

where the Jacobian reads

$$\left|\frac{d\ln M}{d\mu}\right| = \left|\frac{3(1+w)}{1+3w}\frac{d\zeta_{\rm sp}(r_m)}{d\mu} + \frac{\gamma(w)}{\mu - \mu_{\rm c,sp}}\right| \tag{B.4}$$

with $r_m \approx 2.74/k_p$. The PBH mass function, defined as the fraction of PBHs in the form of dark matter at the current time, is finally given by

$$f_{\rm PBH}(M) = \frac{M\,n_{\rm PBH}(M)}{3M_{\rm pl}^2 H_0^2 \Omega_{\rm DM}}. \tag{B.5}$$

Integrating $f_{\rm PBH}(M)$, we can fix $\mathcal{A}_\zeta$ for a desired value of $f_{\rm PBH,tot}$ and infer the value of $\nu_{\rm c}$ using the critical threshold value $\mu_{\rm c,sp}$. To obtain accurately the threshold values $\mu_{\rm c,sp}$,
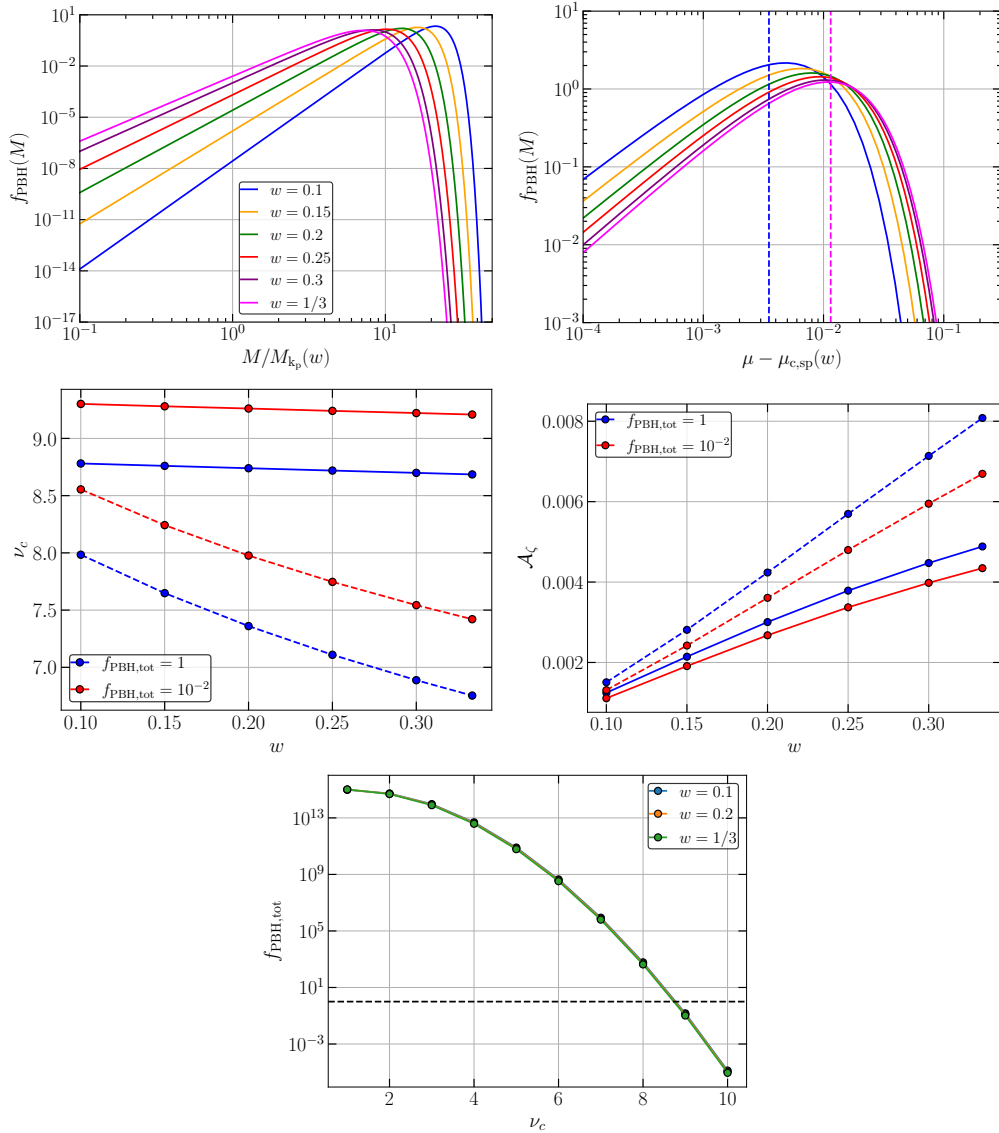
Figure 15. Top panels: PBH mass functions for several values of w with the monochromatic power spectrum as functions of M/M_{k_p} (left) and $\mu - \mu_c$ (right) with $M_{k_p} = (g_\star/106.75)^{-1/6} \cdot 10^{20} \left(k_p/(1.56 \cdot 10^{13} \text{Mpc}^{-1})\right)^{-3(1+w)/(1+3w)} M_\odot$. We fix $k_p = 10^{13.5} \text{Mpc}^{-1}$ (asteroid mass range) with $g_* = 106.75$ in both cases. The dashed vertical lines in the left panel denote the typical values μ_t for $w = 1/10$ and $w = 1/3$ used in the simulations. Middle panels: Critical values of ν_c (left) and the amplitude of the power spectrum $\mathcal{A}_\zeta$ (right) as functions of w. The solid and dashed lines correspond to $k_p = 10^{13.5}$ (asteroid mass range) and $k_p = 10^7$ (solar mass range), respectively, with $g_* = 10.75$. Bottom panel: Value of $f_{\text{PBH}}^{\text{tot}}$ as a function of μ_c for $k_p = 10^{13.5} \text{Mpc}^{-1}$.

relativistic numerical simulations are necessary. We use the SPriBoSH code [74] to compute those values, which were already computed and are shown in Fig. 11 of [10].

In Fig.15 we show the results for several values of w. In the top-left panel, we show the mass functions $f_{\mathrm{PBH}}(M)$ with $f_{\mathrm{PBH}}^{\mathrm{tot}} = 1$. Notice that the slope of the mass function in small M originates from the critical exponent γ of the critical collapse since the mass functions will grow as $f_{\mathrm{PBH}}(M) \sim M^{1+1/\gamma(w)}$ due to the Jacobian term (see Eq. (B.4) with $M \sim (\mu - \mu_{\mathrm{c,sp}})^{\gamma(w)}$ from the critical collapse regime [27, 38, 75, 93, 94]), where the term $\gamma(w)/(\mu - \mu_{\mathrm{c,sp}})$ will become dominant when the fluctuations are in the critical regime $\mu \to \mu_{\mathrm{c,sp}}$. In the top-right panel, we show the same $f_{\mathrm{PBH}}(M)$ but as functions of $\mu - \mu_{\mathrm{c,sp}}(w)$. Notice that the mass function peaks when $\mu - \mu_{\mathrm{c,sp}} \approx 10^{-2}$; we consider these as typical values of the amplitude of fluctuation, where the maximal number of PBHs is produced. In the middle left panel, we show the critical ν_{c} (when $\mu \to \mu_{\mathrm{c,sp}}$), where it is explicitly shown that we need $\nu \gg 1$ (a large peak) to have $f_{\mathrm{PBH}} = 1$. The fact that ν_{c} is increased when the equation of state parameter becomes softer can be understood from the fact that in this scenario, the production of PBHs will be higher due to the threshold reduction, then for the same f_{PBH}, the needed amplitude of the power spectrum will be reduced accordingly (see the middle right panel). Notice that we need $\nu_{\mathrm{c}} \gtrsim 7$ to have $f_{\mathrm{PBH}}^{\mathrm{tot}} \leq 1$ for $w \leq 1/3$. Finally, in the bottom panel, we show an example of how PBHs are overproduced if we consider a lower value ν_{c} (larger value of $\mathcal{A}_\zeta$) for the monochromatic power spectrum.

C Suplemental figures of the gravitational collapse for $w = 1/10$

In this appendix, we present additional figures illustrating the gravitational collapse for the case of $w = 1/10$. Overall, the qualitative behaviour is similar to the cases discussed in section 4.1. We find that the most notable qualitative difference is that the collapse takes longer than in the $w = 1/3$ case, as previously mentioned. Figs.16, 17 and 18 show a scenario where the fluctuation collapses to form a black hole. The initial shape of the fluctuation in the $z - x$ plane is nearly spherical, with eigenvalues $\lambda_1/(\nu\sigma_2) = 1.175$, $\lambda_2/(\nu\sigma_2) = 1.1$, and $\lambda_3/(\nu\sigma_2) = 0.825$, where $\lambda_1 \approx \lambda_2$. In contrast, Figs.16, 17 and 18 depict a case with an initial prolate spheroidal geometry, where the eigenvalues are $\lambda_1/(\nu\sigma_2) = 0.825$, $\lambda_2/(\nu\sigma_2) = 1.35$, and $\lambda_3/(\nu\sigma_2) = 0.825$, with $\lambda_1 = \lambda_3 < \lambda_2$. Although the oscillating behaviour is similar to what was observed previously, it eventually transitions to an oblate geometry, approaching an almost spherical shape in the final stages.

D Convergence of the numerical simulations

In this appendix, we present several figures illustrating the evolution of the Hamiltonian constraint (see [70] for the equations). We compute the averaged Hamiltonian constraint, depicted in Fig.24. Our results indicate that the Hamiltonian constraint is well-satisfied until late times, when the simulation breaks down in some cases, particularly in the radiation-dominated scenarios. In some cases for $w = 1/10$, we terminated the computation once the numerical evolution provided sufficient evidence for either black hole formation or not. Notably, when the Hamiltonian constraint starts to be violated, a bouncing behaviour of the lapse function at the centre can already be observed. This allows us to robustly determine the threshold for black hole formation using a bisection method with different iterations.

---

[6]Notice that for the general case, the relation between $n_{\mathrm{PBH}}(M)$ will involve integration over the variable ξ introduced in section 2, but for the monochromatic power spectrum, this is simply given by $\xi = \nu$.
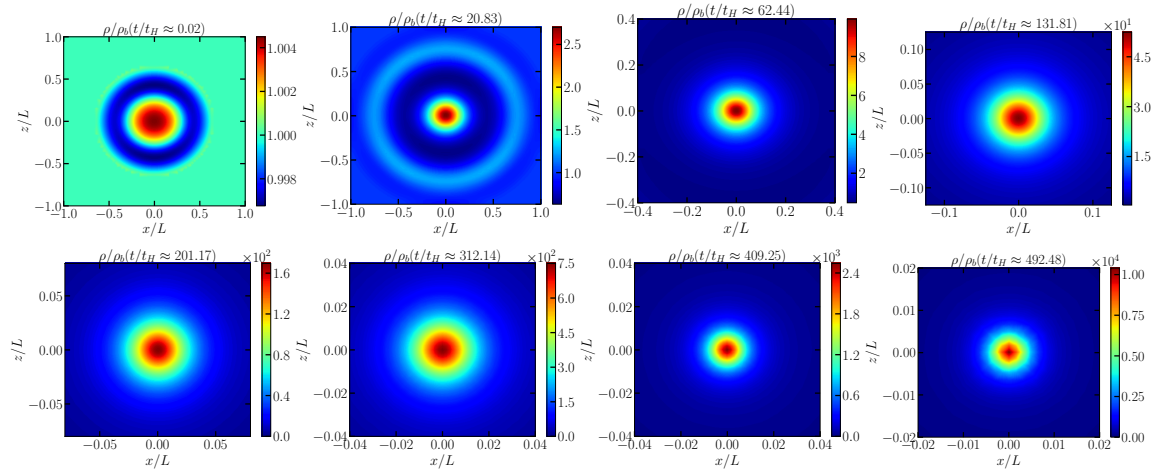
Figure 16. Snapshots of the evolution of ρ/ρ_b in the plane $y = 0$ for $e = 0.075$ and $p = -0.05$ with $w = 1/10$.
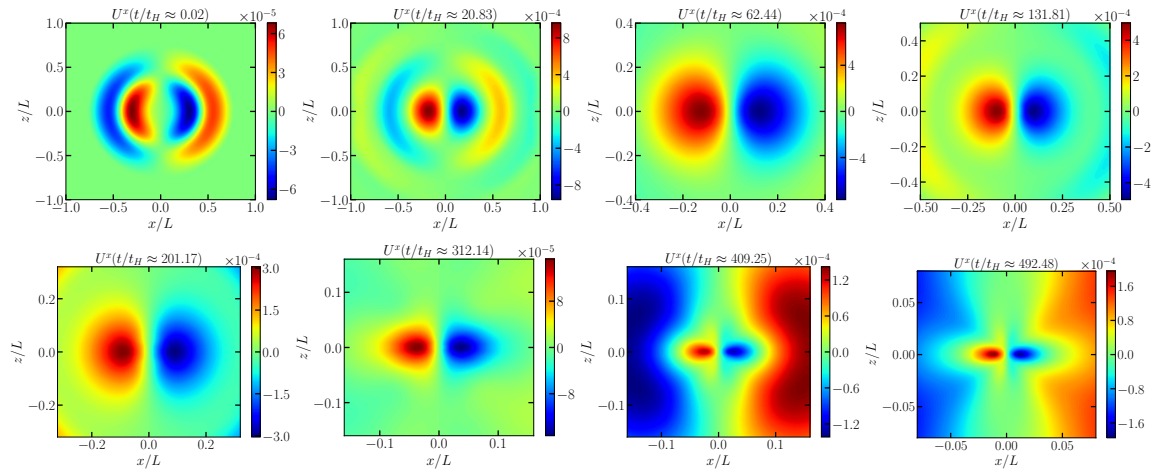

Figure 17. Snapshots of the evolution of the Eulerian velocity U^x in the plane $y = 0$ for $e = 0.075$ and $p = -0.05$ with $w = 1/10$.

References

[1] Y.B. Zel'dovich and I.D. Novikov, *The Hypothesis of Cores Retarded during Expansion and the Hot Cosmological Model*, Soviet Astron. AJ (Engl. Transl.), **10** (1967) 602.

[2] S. Hawking, *Gravitationally Collapsed Objects of Very Low Mass*, *Monthly Notices of the Royal Astronomical Society* **152** (1971) 75 [https://academic.oup.com/mnras/article-pdf/152/1/75/9360899/mnras152-0075.pdf].

[3] B. Carr and S. Hawking, *Black holes in the early Universe*, MNRAS **168** (1974) 399.

[4] B.J. Carr, *The primordial black hole mass spectrum.*, ApJ **201** (1975) 1.

[5] I.D. Novikov, A.G. Polnarev, A.A. Starobinskii and I.B. Zeldovich, *Primordial black holes*, A&A **80** (1979) 104.

[6] M. Sasaki, T. Suyama, T. Tanaka and S. Yokoyama, *Primordial black holes—perspectives in gravitational wave astronomy*, *Class. Quant. Grav.* **35** (2018) 063001 [1801.05235].
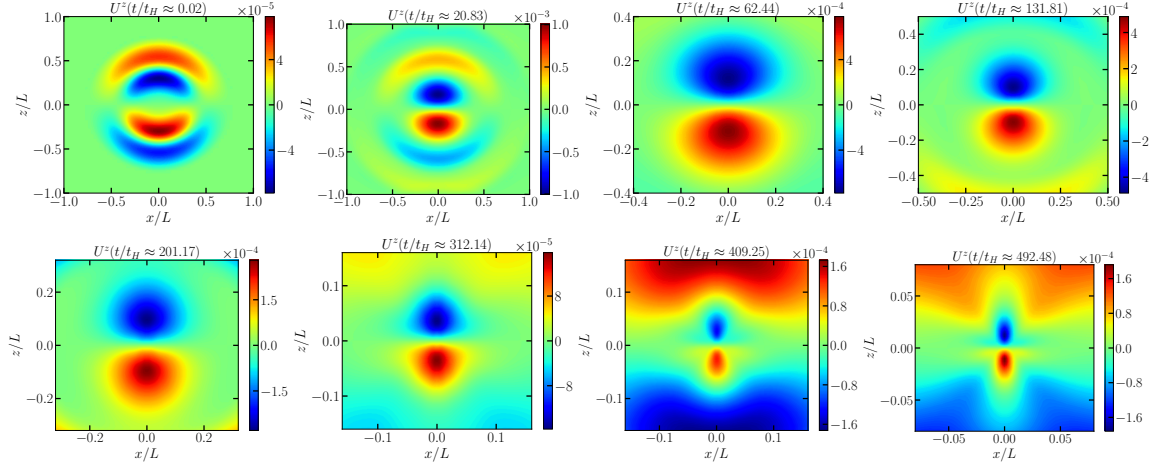
Figure 18. Snapshots of the evolution of the Eulerian velocity U^z in the plane $y = 0$ for $e = 0.075$ and $p = -0.05$ with $w = 1/10$.
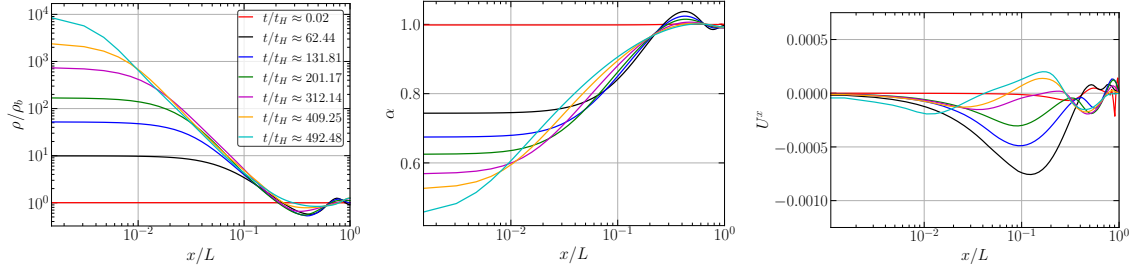

Figure 19. Snapshots of the energy density ρ/ρ_b (left-panel), lapse function α (middle-panel) and Eulerian velocity U^x (right-panel) on the x axis ($y = z = 0$) for $e = 0.08$ and $p = 0$ with $w = 1/10$.
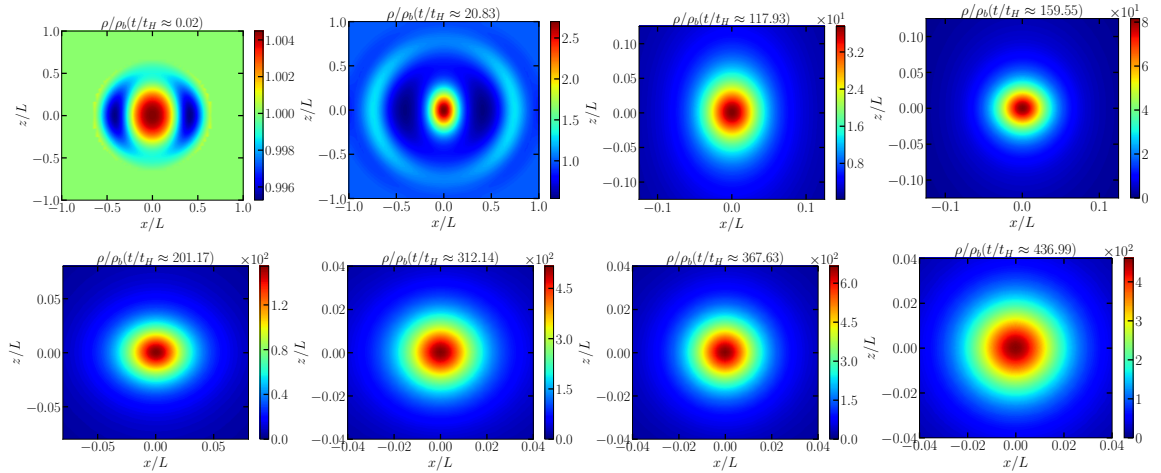

Figure 20. Snapshots of the evolution of ρ/ρ_b in the plane $y = 0$ for $e = 0$ and $p = -0.175$ with $w = 1/10$.
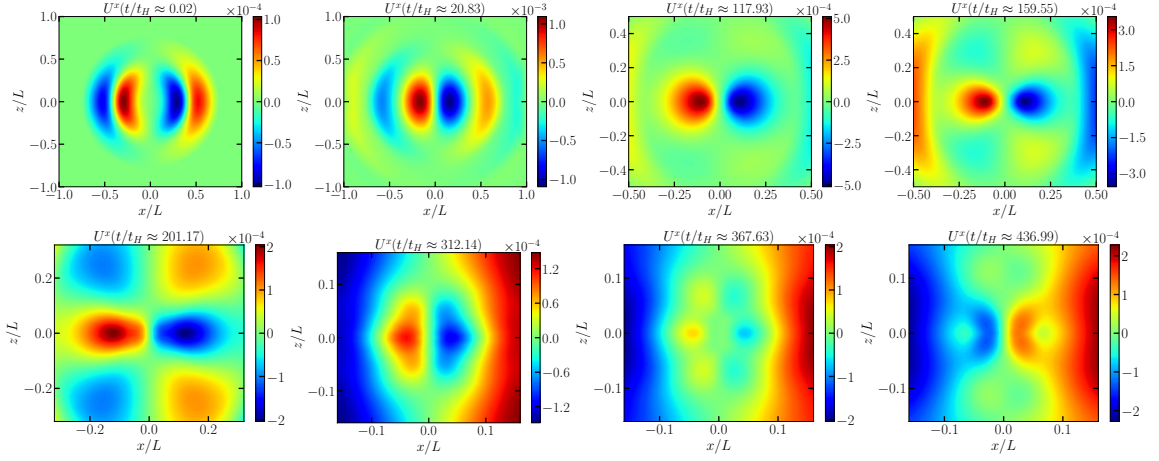
Figure 21. Snapshots of the evolution of the Eulerian velocity U^x in the plane $y = 0$ for $e = 0$ and $p = -0.175$ with $w = 1/10$.
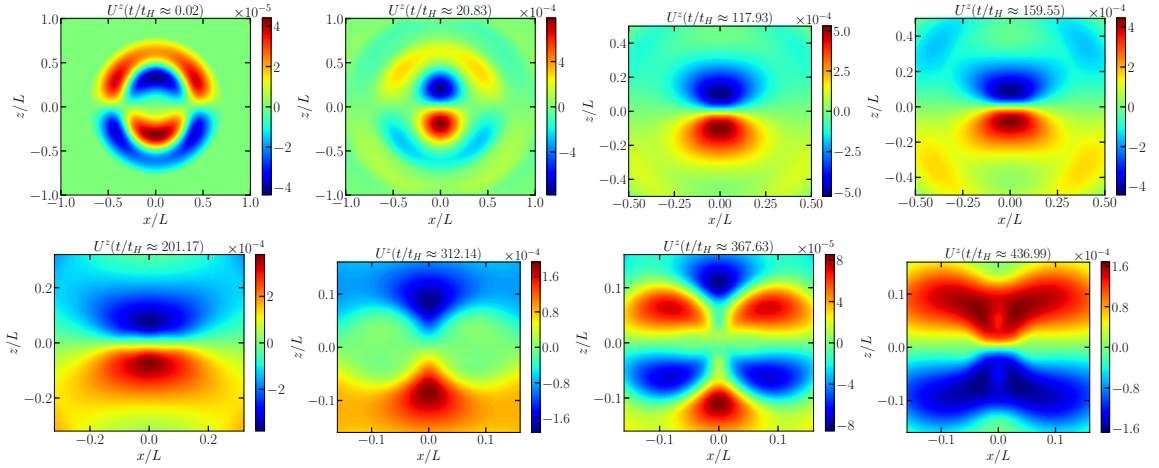

Figure 22. Snapshots of the evolution of the Eulerian velocity U^z in the plane $y = 0$ for $e = 0, p = -0.175$ with $w = 1/10$.
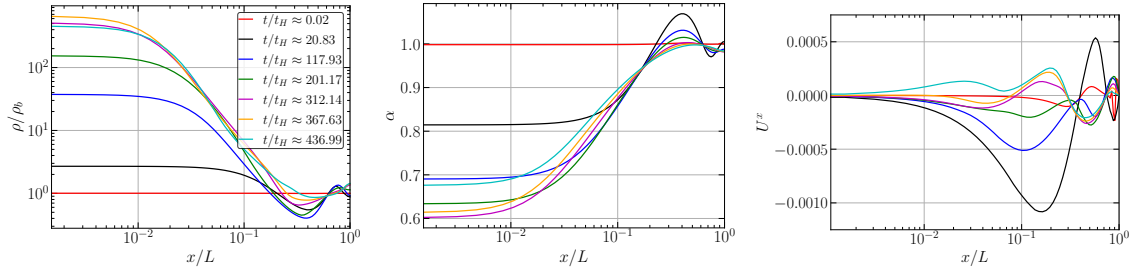

Figure 23. Snapshots of the energy density ρ/ρ_b (left-panel), lapse function α (middle-panel) and Eulerian velocity U^x (right-panel) on the x axis ($y = z = 0$) for $e = 0$ and $p = 0.175$ with $w = 1/10$.
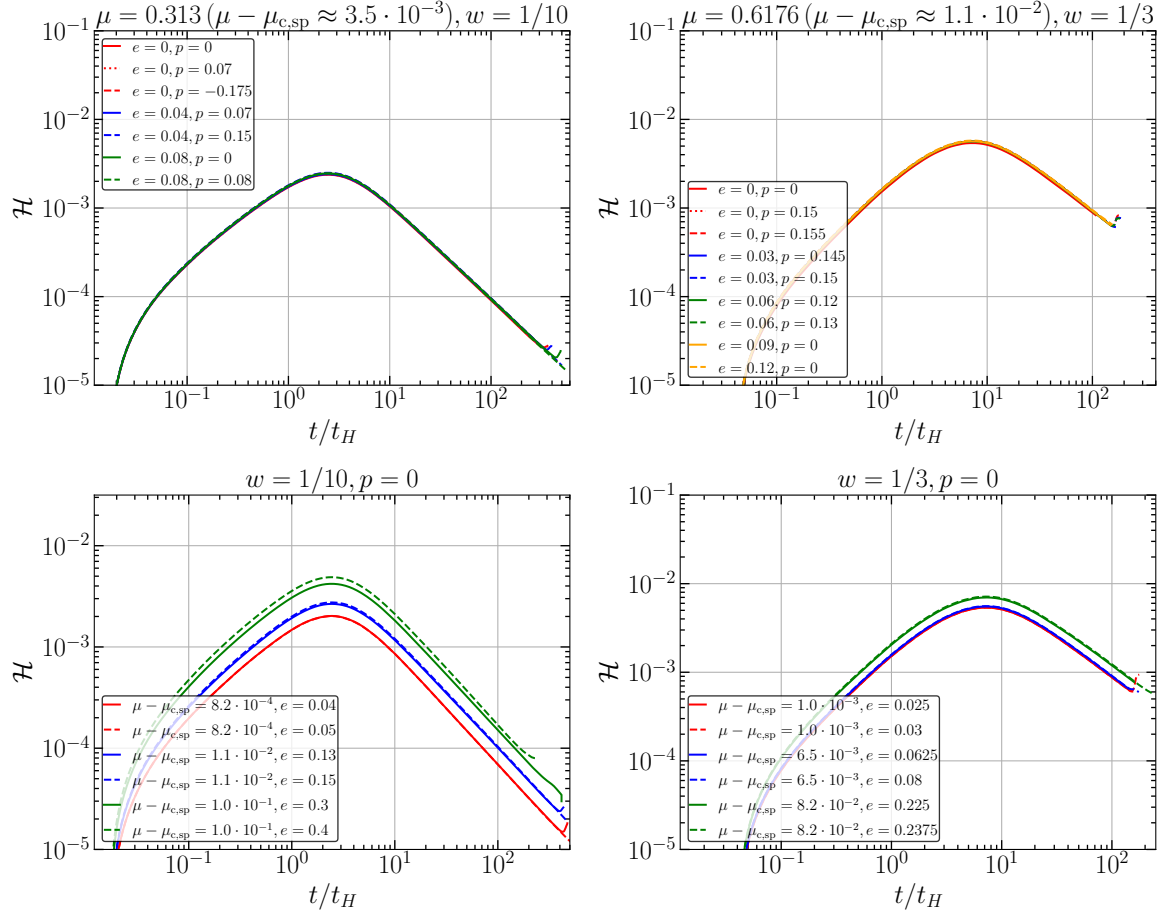
Figure 24. Evolution of the averaged Hamiltonian constraint in time for the cases shown in Fig.11.

[7] A.M. Green and B.J. Kavanagh, *Primordial Black Holes as a dark matter candidate*, *J. Phys. G* **48** (2021) 043001 [2007.10722].

[8] B. Carr, K. Kohri, Y. Sendouda and J. Yokoyama, *Constraints on primordial black holes*, *Rept. Prog. Phys.* **84** (2021) 116902 [2002.12778].

[9] B. Carr and F. Kuhnel, *Primordial Black Holes as Dark Matter: Recent Developments*, *Ann. Rev. Nucl. Part. Sci.* **70** (2020) 355 [2006.02838].

[10] A. Escrivà, F. Kuhnel and Y. Tada, *Primordial Black Holes*, 2211.05767.

[11] C.-M. Yoo, *The Basics of Primordial Black Hole Formation and Abundance Estimation*, *Galaxies* **10** (2022) 112 [2211.13512].

[12] G.F. Chapline, *Cosmological effects of primordial black holes*, *Nature* **253** (1975) 251.

[13] B. Carr, S. Clesse, J. Garcia-Bellido, M. Hawkins and F. Kuhnel, *Observational evidence for primordial black holes: A positivist perspective*, *Phys. Rept.* **1054** (2024) 1 [2306.03903].

[14] M. Sasaki, T. Suyama, T. Tanaka and S. Yokoyama, *Primordial Black Hole Scenario for the Gravitational-Wave Event GW150914*, *Phys. Rev. Lett.* **117** (2016) 061101 [1603.08338].

[15] B. Abbott, others, LIGO Scientific Collaboration and Virgo Collaboration, *Binary Black Hole Mergers in the First Advanced LIGO Observing Run*, *Physical Review X* **6** (2016) 041015 [1606.04856].

[16] R. Abbott, others, The LIGO Scientific Collaboration, the Virgo Collaboration and the KAGRA Collaboration, *GWTC-3: Compact Binary Coalescences Observed by LIGO and Virgo During the Second Part of the Third Observing Run*, *arXiv e-prints* (2021) arXiv:2111.03606 [2111.03606].

[17] A. Escrivà, *PBH Formation from Spherically Symmetric Hydrodynamical Perturbations: A Review*, *Universe* **8** (2022) 66 [2111.12693].

[18] C.-M. Yoo, T. Harada and H. Okawa, *Threshold of Primordial Black Hole Formation in Nonspherical Collapse*, *Phys. Rev. D* **102** (2020) 043526 [2004.01042].

[19] E. de Jong, J.C. Aurrekoetxea and E.A. Lim, *Primordial black hole formation with full numerical relativity*, *JCAP* **03** (2022) 029 [2109.04896].

[20] E. de Jong, J.C. Aurrekoetxea, E.A. Lim and T. França, *Spinning primordial black holes formed during a matter-dominated era*, *JCAP* **10** (2023) 067 [2306.11810].

[21] C.-M. Yoo, *Primordial black hole formation from a nonspherical density profile with a misaligned deformation tensor*, *Phys. Rev. D* **110** (2024) 043526 [2403.11147].

[22] J. Celestino and T.W. Baumgarte, *Critical collapse of ultrarelativistic fluids: Damping or growth of aspherical deformations*, *Phys. Rev. D* **98** (2018) 024053 [1805.10442].

[23] C. Gundlach and T.W. Baumgarte, *Critical gravitational collapse with angular momentum*, *Phys. Rev. D* **94** (2016) 084012 [1608.00491].

[24] T.W. Baumgarte and C. Gundlach, *Critical collapse of rotating radiation fluids*, *Phys. Rev. Lett.* **116** (2016) 221103 [1603.04373].

[25] C. Gundlach and T.W. Baumgarte, *Critical gravitational collapse with angular momentum II: soft equations of state*, *Phys. Rev. D* **97** (2018) 064006 [1712.05741].

[26] J.M. Bardeen, J.R. Bond, N. Kaiser and A.S. Szalay, *The Statistics of Peaks of Gaussian Random Fields*, *Astrophys. J.* **304** (1986) 15.

[27] M.W. Choptuik, *Universality and scaling in gravitational collapse of a massless scalar field*, *Phys. Rev. Lett.* **70** (1993) 9.

[28] A. Escrivà, C. Germani and R.K. Sheth, *Universal threshold for primordial black hole formation*, *Phys. Rev. D* **101** (2020) 044022.

[29] A. Escrivà, C. Germani and R.K. Sheth, *Analytical thresholds for black hole formation in general cosmological backgrounds*, *JCAP* **01** (2021) 030 [2007.05564].

[30] M.Y. Khlopov and A.G. Polnarev, *PRIMORDIAL BLACK HOLES AS A COSMOLOGICAL TEST OF GRAND UNIFICATION*, *Phys. Lett. B* **97** (1980) 383.

[31] T. Harada and S. Jhingan, *Spherical and nonspherical models of primordial black hole formation: exact solutions*, *PTEP* **2016** (2016) 093E04 [1512.08639].

[32] T. Harada, C.-M. Yoo, K. Kohri and K.-I. Nakao, *Spins of primordial black holes formed in the matter-dominated phase of the Universe*, *Phys. Rev. D* **96** (2017) 083517 [1707.03595].

[33] M.Y. Khlopov, B.A. Malomed, I.B. Zeldovich and Y.B. Zeldovich, *Gravitational instability of scalar fields and formation of primordial black holes*, *Mon. Not. Roy. Astron. Soc.* **215** (1985) 575.

[34] J.C. Hidalgo, J. De Santiago, G. German, N. Barbosa-Cendejas and W. Ruiz-Luna, *Collapse threshold for a cosmological Klein Gordon field*, *Phys. Rev. D* **96** (2017) 063504 [1705.02308].

[35] B. Carr, T. Tenkanen and V. Vaskonen, *Primordial black holes from inflaton and spectator field perturbations in a matter-dominated era*, *Phys. Rev. D* **96** (2017) 063507 [1706.03746].

[36] K. Carrion, J.C. Hidalgo, A. Montiel and L.E. Padilla, *Complex Scalar Field Reheating and Primordial Black Hole production*, *JCAP* **07** (2021) 001 [2101.02156].

[37] L.E. Padilla, J.C. Hidalgo and K.A. Malik, *New mechanism for primordial black hole formation during reheating*, *Phys. Rev. D* **106** (2022) 023519 [`2110.14584`].

[38] I. Musco and J.C. Miller, *Primordial black hole formation in the early universe: critical behaviour and self-similarity*, *Class. Quant. Grav.* **30** (2013) 145009 [`1201.2379`].

[39] G. Domènech, *Scalar Induced Gravitational Waves Review*, *Universe* **7** (2021) 398 [`2109.01398`].

[40] T. Nakamura, M. Sasaki, T. Tanaka and K.S. Thorne, *Gravitational waves from coalescing black hole MACHO binaries*, *Astrophys. J. Lett.* **487** (1997) L139 [`astro-ph/9708060`].

[41] Y. Ali-Haïmoud, E.D. Kovetz and M. Kamionkowski, *Merger rate of primordial black-hole binaries*, *Phys. Rev. D* **96** (2017) 123523 [`1709.06576`].

[42] R. Allahverdi et al., *The First Three Seconds: a Review of Possible Expansion Histories of the Early Universe*, `2006.16182`.

[43] C. Schmid, D.J. Schwarz and P. Widerin, *Amplification of cosmological inhomogeneities from the QCD transition*, *Phys. Rev. D* **59** (1999) 043517 [`astro-ph/9807257`].

[44] M. Laine and Y. Schroder, *Quark mass thresholds in QCD thermodynamics*, *Phys. Rev. D* **73** (2006) 085009 [`hep-ph/0603048`].

[45] S. Borsanyi et al., *Calculation of the axion mass based on high-temperature lattice quantum chromodynamics*, *Nature* **539** (2016) 69 [`1606.07494`].

[46] K. Jedamzik, *Primordial black hole formation during the QCD epoch*, *Phys. Rev. D* **55** (1997) 5871 [`astro-ph/9605152`].

[47] P. Widerin and C. Schmid, *Primordial black holes from the QCD transition?*, `astro-ph/9808142`.

[48] J.L.G. Sobrinho, P. Augusto and A.L. Gonçalves, *New thresholds for Primordial Black Hole formation during the QCD phase transition*, *Mon. Not. Roy. Astron. Soc.* **463** (2016) 2348 [`1609.01205`].

[49] C.T. Byrnes, M. Hindmarsh, S. Young and M.R.S. Hawkins, *Primordial black holes with an accurate QCD equation of state*, *JCAP* **08** (2018) 041 [`1801.06138`].

[50] B. Carr, S. Clesse, J. García-Bellido and F. Kühnel, *Cosmic conundra explained by thermal history and primordial black holes*, *Phys. Dark Univ.* **31** (2021) 100755 [`1906.08217`].

[51] K. Jedamzik, *Primordial Black Hole Dark Matter and the LIGO/Virgo observations*, *JCAP* **09** (2020) 022 [`2006.11172`].

[52] S. Clesse and J. Garcia-Bellido, *GW190425, GW190521 and GW190814: Three candidate mergers of primordial black holes from the QCD epoch*, `2007.06481`.

[53] J.I. Juan, P. Serpico and G. Franco Abellán, *The QCD phase transition behind a PBH origin of LIGO/Virgo events?*, `2204.07027`.

[54] G. Franciolini, I. Musco, P. Pani and A. Urbano, *From inflation to black hole mergers and back again: Gravitational-wave data-driven constraints on inflationary scenarios with a first-principle model of primordial black holes across the QCD epoch*, *Phys. Rev. D* **106** (2022) 123526 [`2209.05959`].

[55] A. Escrivà, E. Bagui and S. Clesse, *Simulations of PBH formation at the QCD epoch and comparison with the GWTC-3 catalog*, *JCAP* **05** (2023) 004 [`2209.06196`].

[56] A. Escrivà and J.G. Subils, *Primordial black hole formation during a strongly coupled crossover*, *Phys. Rev. D* **107** (2023) L041301 [`2211.15674`].

[57] A. Escrivà, Y. Tada and C.-M. Yoo, *Primordial Black Holes and Induced Gravitational Waves from a Smooth Crossover beyond Standard Model*, `2311.17760`.

[58] NANOGRAV collaboration, *The NANOGrav 15 yr Data Set: Search for Signals from New Physics*, *Astrophys. J. Lett.* **951** (2023) L11 [2306.16219].

[59] EPTA collaboration, *The second data release from the European Pulsar Timing Array: IV. Implications for massive black holes, dark matter and the early Universe*, 2306.16227.

[60] G. Domènech and S. Pi, *NANOGrav hints on planet-mass primordial black holes*, *Sci. China Phys. Mech. Astron.* **65** (2022) 230411 [2010.03976].

[61] L. Liu, Y. Wu and Z.-C. Chen, *Simultaneously probing the sound speed and equation of state of the early Universe with pulsar timing arrays*, *JCAP* **04** (2024) 011 [2310.16500].

[62] L. Liu, Z.-C. Chen and Q.-G. Huang, *Probing the equation of state of the early Universe with pulsar timing arrays*, *JCAP* **11** (2023) 071 [2307.14911].

[63] K. Harigaya, K. Inomata and T. Terada, *Induced gravitational waves with kination era for recent pulsar timing array signals*, *Phys. Rev. D* **108** (2023) 123538 [2309.00228].

[64] S. Choudhury, K. Dey and A. Karde, *Untangling PBH overproduction in w-SIGWs generated by Pulsar Timing Arrays for MST-EFT of single field inflation*, 2311.15065.

[65] G. Domènech, S. Pi, A. Wang and J. Wang, *Induced Gravitational Wave interpretation of PTA data: a complete study for general equation of state*, 2402.18965.

[66] S. Choudhury, A. Karde, S. Panda and M. Sami, *Realisation of the ultra-slow roll phase in Galileon inflation and PBH overproduction*, *JCAP* **07** (2024) 034 [2401.10925].

[67] V. Atal, J. Cid, A. Escrivà and J. Garriga, *PBH in single field inflation: the effect of shape dispersion and non-Gaussianities*, J. Cosmology Astropart. Phys. **2020** (2020) 022 [1908.11357].

[68] M. Shibata and T. Nakamura, *Evolution of three-dimensional gravitational waves: Harmonic slicing case*, *Phys. Rev. D* **52** (1995) 5428.

[69] T.W. Baumgarte and S.L. Shapiro, *On the numerical integration of Einstein's field equations*, *Phys. Rev. D* **59** (1998) 024007 [gr-qc/9810065].

[70] T. Harada, C.-M. Yoo, T. Nakama and Y. Koga, *Cosmological long-wavelength solutions and primordial black hole formation*, *Phys. Rev. D* **91** (2015) 084057 [1503.03934].

[71] C.-M. Yoo and H. Okawa, *Black hole universe with a cosmological constant*, *Phys. Rev. D* **89** (2014) 123502 [1404.1435].

[72] H. Okawa, H. Witek and V. Cardoso, *Black holes and fundamental fields in Numerical Relativity: initial data construction and evolution of bound states*, *Phys. Rev. D* **89** (2014) 104032 [1401.1548].

[73] T. Yamamoto, M. Shibata and K. Taniguchi, *Simulating coalescing compact binaries by a new code SACRA*, *Phys. Rev. D* **78** (2008) 064054 [0806.4007].

[74] A. Escrivà, *Simulation of primordial black hole formation using pseudo-spectral methods*, *Physics of the Dark Universe* **27** (2020) 100466.

[75] J.C. Niemeyer and K. Jedamzik, *Dynamics of primordial black hole formation*, *Phys. Rev. D* **59** (1999) 124013 [astro-ph/9901292].

[76] I. Musco, J.C. Miller and L. Rezzolla, *Computations of primordial black hole formation*, *Class. Quant. Grav.* **22** (2005) 1405 [gr-qc/0412063].

[77] C.-M. Yoo, T. Harada, S. Hirano, H. Okawa and M. Sasaki, *Primordial black hole formation from massless scalar isocurvature*, Phys. Rev. D **105** (2022) 103538 [2112.12335].

[78] K. Uehara, A. Escrivà, T. Harada, D. Saito and C.-M. Yoo, *Numerical simulation of type II primordial black hole formation*, 2401.06329.

[79] M. Shibata and M. Sasaki, *Black hole formation in the Friedmann universe: Formulation and computation in numerical relativity*, *Phys. Rev. D* **60** (1999) 084002 [`gr-qc/9905064`].

[80] A. Escrivà and A.E. Romano, *Effects of the shape of curvature peaks on the size of primordial black holes*, *JCAP* **05** (2021) 066 [`2103.03867`].

[81] A. Escrivà and C.-M. Yoo, *Primordial Black hole formation from overlapping cosmological fluctuations*, *JCAP* **04** (2024) 048 [`2310.16482`].

[82] N. Kitajima, Y. Tada, S. Yokoyama and C.-M. Yoo, *Primordial black holes in peak theory with a non-Gaussian tail*, *JCAP* **10** (2021) 053 [`2109.00791`].

[83] T.W. Baumgarte and P.J. Montero, *Critical phenomena in the aspherical gravitational collapse of radiation fluids*, *Phys. Rev. D* **92** (2015) 124065 [`1509.08730`].

[84] K. Marouda, D. Cors, H.R. Rüter, F. Atteneder and D. Hilditch, *Twist-free axisymmetric critical collapse of a complex scalar field*, *Phys. Rev. D* **109** (2024) 124042 [`2402.06724`].

[85] A. Escrivà and C.-M. Yoo, *Non-spherical effects on the mass function of Primordial Black Holes*, `2410.03451`.

[86] C.C. Lin, L. Mestel and F.H. Shu, *The Gravitational Collapse of a Uniform Spheroid.*, *ApJ* **142** (1965) 1431.

[87] Y.B. Zel'dovich, *Gravitational instability: An approximate theory for large density perturbations.*, A&A **5** (1970) 84.

[88] T. Harada, C.-M. Yoo, K. Kohri, K.-i. Nakao and S. Jhingan, *Primordial black hole formation in the matter-dominated phase of the Universe*, *Astrophys. J.* **833** (2016) 61 [`1609.01588`].

[89] T. Harada, K. Kohri, M. Sasaki, T. Terada and C.-M. Yoo, *Threshold of primordial black hole formation against velocity dispersion in matter-dominated era*, *JCAP* **02** (2023) 038 [`2211.13950`].

[90] K.S. Thorne, *"Nonspherical Gravitational Collapse: A Short Review" in Magic without Magic*, ed. J Klauder (San Francisco: Freeman) (1972) .

[91] C.-M. Yoo, T. Harada, J. Garriga and K. Kohri, *Primordial black hole abundance from random Gaussian curvature perturbations and a local density threshold*, *PTEP* **2018** (2018) 123E01 [`1805.03946`].

[92] C.-M. Yoo, T. Harada, S. Hirano and K. Kohri, *Abundance of Primordial Black Holes in Peak Theory for an Arbitrary Power Spectrum*, *PTEP* **2021** (2021) 013E02 [`2008.02425`].

[93] C.R. Evans and J.S. Coleman, *Observation of critical phenomena and selfsimilarity in the gravitational collapse of radiation fluid*, *Phys. Rev. Lett.* **72** (1994) 1782 [`gr-qc/9402041`].

[94] T. Koike, T. Hara and S. Adachi, *Critical behavior in gravitational collapse of radiation fluid: A Renormalization group (linear perturbation) analysis*, *Phys. Rev. Lett.* **74** (1995) 5170 [`gr-qc/9503007`].